Monthly Notices of the ROYAL ASTRONOMICAL SOCIETY

MNRAS **507,** 5952–5973 (2021) https://doi.org/10.1093/mnras/stab2321
Advance Access publication 2021 August 12

2D surface brightness modelling of large 2MASS galaxies – I: photometry and structural parameters

Emmanuel Ríos-López [1,2★] Christopher Añorve [2★] Héctor J. Ibarra-Medel [1,3] Omar López-Cruz [1] Joaquín Alvira-Enríquez,[4] Gabriela Iacobuta[5,6,7] and Mabel Valerdi[1,8]

[1]*Instituto Nacional de Astrofísica, Óptica y Electrónica, Luis Enrique Erro 1, 72840, Tonantzintla, Puebla, México*
[2]*Facultad de Ciencias de la Tierra y el Espacio, Universidad Autónoma de Sinaloa, Av. Universitarios, Cd. Universitaria, 80040, Culiacán, Sinaloa, México*
[3]*Department of Astronomy, University of Illinois Urbana–Champaign, 1002 West Green Street, Urbana, IL 61801, USA*
[4]*Department of Physics, Universidad Iberoamericana, Prol. Paseo de la Reforma 880, 01219, México DF, México*
[5]*School of Physics and Astronomy, University of Nottingham, Nottingham NG7 2RD, UK*
[6]*German Development Institute/Deutsches Institut fur Entwicklungspolitik (GDI/DIE), Tulpenfeld 6, D-53113 Bonn, Germany*
[7]*Environmental Systems Analysis Group, Wageningen University & Research, PO Box 47, NL-6700 AA Wageningen, the Netherlands*
[8]*Instituto de Astronomía, Universidad Nacional Autónoma de México, Avenida Universidad 3000, Ciudad Universitaria, C.P. 04510, Mexico DF, México*

Accepted 2021 August 6. Received 2021 July 21; in original form 2020 December 15

ABSTRACT

We have studied a sample of 101 bright 2MASS galaxies from the Large Galaxy Atlas (LGA), whose morphologies span from early to late types. We have generated estimates for structural parameters through a two-dimensional surface brightness photometric decomposition in the three 2MASS bands (J, H, and K_s). This work represents a detailed multicomponent photometric study of nearby galaxies. We report total magnitudes, effective radii, and concentration indices, among other parameters, in the three 2MASS bands. We found that the integrated total magnitudes of early-type galaxies (ETGs) measured on 2MASS LGA mosaics are ∼0.35 mag dimmer, when compared with images generated from IRSA image tile service; nevertheless, when comparing late-type galaxies (LTGs) we did not find any difference. Therefore, for ETGs we present the results derived on IRSA image tiles, while for LTGs we used data from the LGA mosaics. Additionally, by combining these structural parameters with scaling relations and kinematic data, we separated classical bulges from pseudo-bulges. We found that ∼40 per cent of the objects in our sample are classified as pseudo-bulges, which are found preferentially in LTGs. Also, our findings confirm trends reported earlier in the distributions for some physical parameters, such as Sérsic index and B/T and q ratios. In general, our results are in agreement with previous one-dimensional studies. In a companion paper, we revise some of the scaling relations among global galaxy properties, as well as their interrelation with Supermassive Black Holes.

Key words: techniques: photometric – galaxies: bulges – galaxies: fundamental parameters – galaxies: structure.

1 INTRODUCTION

The generally accepted cold dark matter (CDM) scenario is based on a hierarchical galaxy formation model (e.g. White & Rees 1978). If dark energy is included, then we have the general Lambda CDM framework (see e.g. Springel et al. 2005; Spergel et al. 2007), which satisfactorily explains galaxy formation and evolution. Nevertheless, complementary physical processes must be included through semi-analytical approaches (e.g. Silk, Di Cintio & Dvorkin 2015) to have a comprehensive view of such mechanisms.

The morphological classification of galaxies suggests the presence of a common process that takes place during galaxy formation and evolution. However, the photometric structural analysis of galaxies provides qualitative information that supports galaxy classification schemes, which also helps us to constrain the dynamical modelling of galaxies (e.g. Binney, Davies & Illingworth 1990; van der Marel 1991; Cappellari et al. 2013). Moreover, Peebles (2020) suggested that the distribution of the bulge-to-disc ratio in nearby galaxies can help us to constrain cosmological initial conditions. Hence, the accurate modelling of the surface brightness of galaxies acquires additional relevance.

The space of parameters relating dynamics, surface brightness, and scale size can be reduced to conform to the Fundamental Plane (FP; Djorgovski & Davis 1987). Some previously established correlations such as the Faber–Jackson (Faber & Jackson 1976), Kormendy (Kormendy 1977), and the Tully–Fisher (Tully & Fisher 1977) could be considered projections of the FP. These correlations might suggest that other connections among galaxy properties might be present.

Observations of nearby galaxies allow us to attain large angular resolution, which in turn allows us to analyse the distribution of internal structures such as bulges, spiral arms, bars, and rings, among others. The study of those structures in large galaxy samples has helped us to learn that smaller bulges are similar to low-mass compact elliptical galaxies in the local Universe, while larger bulges are equivalent to the massive compact galaxies in the distant Universe (e.g. Dullo & Graham 2013).

As stated above, bulges have become very relevant due to their linkages with the different mechanisms of formation and evolution of galaxies (e.g. Athanassoula 2005). Bulges can be divided into

★ E-mail riloemm@inaoep.mx (ERL); canorve@uas.edu.mx (CA)

two classes established observationally: classical bulges and pseudo-bulges (Kormendy, Bender & Cornell 2011). Classical bulges resemble E galaxies and share some physical aspects; for example, they are systems dominated by velocity dispersions, have a higher Sérsic index (usually above 2), and are populated by old stars. Besides, classical bulges follow the same scaling relations traced by ellipticals. This tells us about their formation history, which is also related to the merger scenario as early-type galaxies (ETGs). On the other hand, pseudo-bulges are more disc-like systems and different from classical and E galaxies. Thus, pseudo-bulges are systems that display more flattening as discs, as well as they are dominated by rotation velocities and tend to have lower Sérsic indices, and young stars are the dominant population. The formation of pseudo-bulges is attributed to secular processes (see Kormendy & Kennicutt 2004; Kormendy & Ho 2013, for reviews about properties of bulge types).

We have employed a two-dimensional (2D) approach to modelling the light distribution of 101 galaxies observed in the near-infrared (NIR), while many studies have been based on one-dimensional (1D) surface photometry to estimate structural parameters (e.g. Peng et al. 2010; Schombert & Smith 2012, and references therein). 1D methods, like isophotal analysis, are suitable for working in poor signal-to-noise ratio (S/N) conditions, since the points on the light profile are the result of the azimuthally averaged surface brightness along the ellipse, as well as the fact that the additional components for each isophote can be known in a relatively direct and easy way (e.g. Jedrzejewski 1987). A drawback of this procedure is that in the presence of multiple galaxy components with different orientations, the selection of major or minor axis could be inaccurate. On the other hand, 2D decomposition methods have the advantage that they are able to disentangle among galaxy components, such as bulges, discs, and bars, breaking part of the degeneracy in the parameters due to the fact that those components may have different ellipticities and position angles. In addition, the 2D approach can provide superior capabilities by convolving the model with the point spread function (PSF). However, a weakness in this case is related to the fact that perfect ellipsoid models may not be entirely appropriate for describing those galaxies with isophotal twists. The differences between 1D and 2D techniques have been widely discussed in the literature (e.g. Ravindranath et al. 2001; Peng et al. 2010; Bonfini 2014; Gao & Ho 2017, and references therein).

Some previous photometric studies have been limited to only two components: discs and bulges, disregarding bars (e.g. Simard et al. 2011). Not including bars may alter the outcome of the decomposition (mainly in magnitude, effective radius, and Sérsic index), related to the overestimation and uncertainties of such values (e.g. Laurikainen et al. 2004a; Fisher & Drory 2008; Gadotti 2008; Méndez-Abreu et al. 2017). Other studies have held some parameters fixed during the fit, for instance the Sérsic index n (e.g. Bruce et al. 2012). This practice affects the estimation of parameters and their errors, as well as the convergence of fits (e.g. Peng et al. 2010). Nevertheless, in the optical there have been some recent 2D studies that include multiple components overcoming the difficulties mentioned above, specifically the work by the group associated with Carnegie–Irvine Galaxy Survey (CGS; e.g. Huang et al. 2013a; Gao & Ho 2017; Gao et al. 2019). Complementary to the CGS results, we present the results of an unrestricted 2D multicomponent NIR photometric study of nearby galaxies, using data from Two Micron All Sky Survey (2MASS; Skrutskie et al. 2006). Our sample includes early-type (E and S0) and late-type (S, SAB, and SB) galaxies. We have used GALFIT (Peng et al. 2002, 2010), allowing three initial components: bulges, discs, and bars; in some cases, an additional PSF component was considered when dealing with active galactic nuclei (AGNs). A comprehensive discussion on the applicability of different models is presented.

Surface brightness studies conducted in the NIR are less affected by gas and dust extinction. Moreover, the galaxies' light in the NIR is dominated by the older stellar populations, which represent the main baryonic component in most galaxies. Hence, NIR observations enhance the contrast between the underlying mass component (older stellar population) and the younger stellar population components, whose light dominates in the optical bands (e.g. Rix & Rieke 1993; de Jong 1996a, b; Frogel, Quillen & Pogge 1996; Jarrett et al. 2003).

The paper is organized as follows: Section 2 describes the sample and the NIR observations from the 2MASS survey, as well as additional data used in this work. In Section 3, we present our methodology, mainly the 2D multicomponent photometric decomposition performed with GALFIT. Section 4 presents the results obtained from surface brightness modelling of the galaxies in the NIR bands of 2MASS, as well as the classification performed to separate bulge types. In Section 5, we discuss our findings. We present our conclusions in Section 6. We also have explored some galaxy scaling relations using the physical properties derived here, along with kinematic data taken from the literature, as well as relations between host galaxy properties and their supermassive black holes (SMBHs). Such results are presented and discussed in a companion paper (Ríos-López et al., in preparation, hereafter Paper II). Unless stated otherwise, we have adopted $\Omega_{\rm m} = 0.3$, $\Omega_{\Lambda} = 0.7$, and $H_0 = 70\,h_{70}$ km s^{-1} Mpc^{-1} throughout the paper.

2 DATA

2.1 Sample and observations

Table 1 presents the sample considered in this study. It contains 101 galaxies, which is a subsample of the 2MASS (Skrutskie et al. 2006) Large Galaxy Atlas[1] (LGA; Jarrett et al. 2003). We have selected some of the nearest ($z \leq 0.01$) and brightest ($K_s \leq 10$) sources in the 2MASS survey (Jarrett 2004). In Fig. 1, we present the distribution according to morphological type, magnitude in the K_s band and redshift.[2] Furthermore, about half of our objects are part of the 100 largest galaxies in angular size observed with 2MASS (Jarrett et al. 2003); some of them can also be found in the 'Atlas de Galaxias Australes' by José Luis Sérsic (1968).

The 2MASS survey began operations in the mid-1990s, completing its observations by early 2001. 2MASS used twin 1.3-m aperture telescopes located in both equatorial hemispheres (the northern telescope at the summit of Mt. Hopkins, Arizona, while the southern telescope at the summit of Cerro Tololo, Chile) to survey the whole sky, detecting more than 500 million stars (Point Source Catalog) and resolving more than 1.5 million galaxies (Extended Source Catalog, XSC) in the NIR bands (Jarrett 2004). 2MASS observed the sky in a drift-scan mode with $8\farcm5 \times 6^{\circ}$ tiles or 'scans', forming 23 separate images per tile per band of $8\farcm5 \times 17'$ coadds. Each image is obtained from six pointings with a total integration time ($t_{\rm int}$) of 7.8 s per pixel, with a plate scale of 1 arcsec per pixel (for more details, see Skrutskie et al. 1997, 2006).

[1]LGA data available at https://irsa.ipac.caltech.edu/applications/2MASS/LGA/atlas.html.

[2]Redshift data from the NASA/IPAC Extragalactic Database (NED) at http://ned.ipac.caltech.edu/. NED is funded by the National Aeronautics and Space Administration and operated by the California Institute of Technology.

Table 1. Sample of large 2MASS galaxies.

Name	Hubble type	v_h (km s^{-1})	Dist. (Mpc)	K_s (2MASS)	K_s	M_{K_s}	σ (km s^{-1})
(1)	(2)	(3)	(4)	(5)	(6)	(7)	(8)
				E + S0 galaxies			
M110	E5;pec	− 241 ± 3	0.82	5.59 ± 0.04	4.67 ± 0.06	− 19.90 ± 0.06	23 ± 4 [a]
M32	cE2	− 213 ± 2	0.80	5.10 ± 0.02	5.08 ± 0.05	− 19.45 ± 0.05	72 ± 2 [a]
Maffei1	S0-pec	66 ± 5	2.85	4.68 ± 0.02	4.43 ± 0.07	− 22.84 ± 0.07	187 ± 6 [b]
NGC 1549	E0-1	1256 ± 12	16.63	6.78 ± 0.02	6.51 ± 0.06	− 24.59 ± 0.06	199 ± 4 [b]
NGC 1947	S0-pec	1100 ± 24	16.30	7.51 ± 0.03	6.86 ± 0.06	− 24.20 ± 0.06	173 ± 12 [a]
NGC 2768	S0;1/2	1353 ± 5	20.46	7.00 ± 0.03	6.80 ± 0.06	− 24.76 ± 0.06	182 ± 4 [a]
NGC 3115	S0-	663 ± 4	9.54	5.88 ± 0.02	5.67 ± 0.05	− 24.22 ± 0.05	252 ± 6 [a]
NGC 3377	E5-6	665 ± 2	10.99	7.44 ± 0.03	7.26 ± 0.09	− 22.94 ± 0.09	139 ± 3 [a]
M105	E1	911 ± 2	10.70	6.27 ± 0.02	6.23 ± 0.04	− 23.92 ± 0.04	207 ± 2 [a]
NGC 4125	E6;pec	1281 ± 14	22.76	6.86 ± 0.02	5.87 ± 0.07	− 25.92 ± 0.07	227 ± 8 [a]
NGC 4365	E3	1243 ± 5	21.62	6.64 ± 0.03	6.26 ± 0.07	− 25.41 ± 0.07	256 ± 3[a]
M86	S0(3)/E3	− 224 ± 5	16.40	6.10 ± 0.03	5.18 ± 0.06	− 25.89 ± 0.06	235 ± 3 [a]
M49	E2/S0(2)	981 ± 5	16.72	5.40 ± 0.02	5.36 ± 0.04	− 25.76 ± 0.04	291 ± 3 [a]
M87	E+0-1pec	1284 ± 5	16.68	5.81 ± 0.02	5.66 ± 0.05	− 25.45 ± 0.05	332 ± 5 [a]
NGC 4636	E/S0$_1$	938 ± 4	13.70	6.42 ± 0.04	5.46 ± 0.05	− 25.22 ± 0.05	203 ± 3 [a]
M60	E2	1110 ± 5	16.46	5.74 ± 0.02	5.25 ± 0.05	− 25.83 ± 0.05	335 ± 4 [a]
NGC 4697	E6	1241 ± 2	12.54	6.37 ± 0.03	5.91 ± 0.07	− 24.58 ± 0.07	172 ± 6 [b]
NGC 4976	E4;pec	1453 ± 24	12.18	6.85 ± 0.02	6.23 ± 0.06	− 24.20 ± 0.06	139 ± 13 [b]
NGC 5084	S0	1721 ± 3	41.37	7.06 ± 0.03	6.93 ± 0.05	− 26.15 ± 0.05	201 ± 6 [b]
IC5328	E	3137 ± 13	37.80	8.28 ± 0.03	8.08 ± 0.12	− 24.81 ± 0.12	206 ± 8 [b]
				S galaxies			
M31	SA(s)b	− 301 ± 1	0.77	0.98 ± 0.02	0.87 ± 0.04	− 23.58 ± 0.04	170 ± 5 [a]
M33	SA(s)cd	− 180 ± 1	0.82	4.10 ± 0.04	3.94 ± 0.06	− 20.63 ± 0.06	21 ± 3 [a]
NGC 1553	SA(rl)0	1080 ± 11	18.40	6.28 ± 0.02	6.26 ± 0.04	− 25.06 ± 0.04	186 ± 4 [b]
NGC 2541	SA(s)cd	548 ± 1	11.50	10.09 ± 0.05	9.37 ± 0.04	− 20.93 ± 0.04	53 ± 10 [a]
NGC 2683	SA(rs)b	411 ± 1	11.70	6.33 ± 0.02	6.23 ± 0.02	− 24.11 ± 0.02	130 ± 7[a]
NGC 2775	SA(r)ab	1350 ± 2	17.00	7.06 ± 0.02	7.01 ± 0.05	− 24.14 ± 0.05	174 ± 8 [a]
NGC 2985	SA(rs)ab	1324 ± 1	20.60	7.36 ± 0.03	7.34 ± 0.03	− 24.23 ± 0.03	141 ± 5 [a]
M81	SA(s)ab;Sy	− 39 ± 3	3.60	3.83 ± 0.02	3.80 ± 0.03	− 23.98 ± 0.03	162 ± 3 [a]
NGC 3631	SA(s)c	1156 ± 1	8.69	7.98 ± 0.06	7.70 ± 0.05	− 21.99 ± 0.05	44 ± 9 [a]
NGC 3675	SA(s)b	770 ± 1	12.40	6.86 ± 0.02	6.83 ± 0.05	− 23.63 ± 0.05	108 ± 4 [a]
NGC 3877	Sc	895 ± 1	15.20	7.75 ± 0.02	7.68 ± 0.05	− 23.23 ± 0.05	86 ± 9 [a]
NGC 3938	SA(s)c	808 ± 2	17.90	7.81 ± 0.05	7.79 ± 0.06	− 23.48 ± 0.06	29 ± 5 [a]
NGC 4013	SAb	831 ± 1	17.80	7.63 ± 0.02	7.58 ± 0.04	− 23.67 ± 0.04	86 ± 9 [a]
NGC 4254	SA(s)c	2406 ± 1	14.30	6.93 ± 0.03	6.72 ± 0.04	− 24.06 ± 0.04	83 ± 9 [a]
M85	SA(s)0;pec	729 ± 2	17.90	6.14 ± 0.02	6.12 ± 0.04	− 25.16 ± 0.04	179 ± 5 [a]
M88	SA(rs)b	2284 ± 1	16.50	6.27 ± 0.02	6.26 ± 0.05	− 24.83 ± 0.05	167 ± 7 [a]
M104	SA(s)a;Sy	1024 ± 5	9.87	4.96 ± 0.02	4.95 ± 0.02	− 25.13 ± 0.02	241 ± 4 [a]
NGC 4710	SA(r)0+	1102 ± 5	16.80	7.57 ± 0.02	7.55 ± 0.04	− 23.81 ± 0.04	110 ± 10 [a]
NGC 4826	SA(rs)ab;Sy	409 ± 1	7.27	5.33 ± 0.02	5.31 ± 0.04	− 24.00 ± 0.04	96 ± 3 [a]
NGC 4866	SA(r)0+sp	1980 ± 3	31.10	7.92 ± 0.02	5.97 ± 0.06	− 24.80 ± 0.06	210 ± 8 [a]
NGC 5033	SA(s)c	875 ± 1	19.30	6.96 ± 0.03	6.94 ± 0.02	− 24.49 ± 0.02	151 ± 4 [a]
M63	SA(rs)bc	500 ± 1	8.90	5.61 ± 0.02	5.55 ± 0.03	− 24.20 ± 0.03	117 ± 6 [a]
NGC 5102	SA0-	468 ± 2	3.20	6.92 ± 0.04	6.90 ± 0.05	− 20.64 ± 0.05	66 ± 10 [b]
M51a	SA(s)bc	460 ± 2	7.90	5.50 ± 0.02	5.35 ± 0.05	− 24.13 ± 0.05	96 ± 9 [a]
NGC 5317	SA(rs)bc;pec	1268 ± 2	13.60	7.80 ± 0.05	7.69 ± 0.11	− 22.97 ± 0.11	22 ± 9 [b]
NGC 6015	SA(s)cd	833 ± 1	18.90	8.47 ± 0.04	8.40 ± 0.06	− 22.98 ± 0.06	44 ± 9 [a]
NGC 6503	SA(s)cd	25 ± 1	5.30	7.30 ± 0.02	7.28 ± 0.05	− 21.34 ± 0.05	46 ± 3 [a]
NGC 7793	SA(s)d	227 ± 2	3.40	6.86 ± 0.06	6.80 ± 0.06	− 20.85 ± 0.06	–
				SAB galaxies			
NGC 253	SAB(s)c	242 ± 1	3.50	3.77 ± 0.02	3.76 ± 0.05	− 23.97 ± 0.05	109 ± 20 [b]
NGC 1316	SAB(s)0	− 107 ± 8	20.95	5.59 ± 0.02	5.48 ± 0.02	− 26.12 ± 0.02	219 ± 10 [b]
IC342	SAB(rs)cd	31 ± 3	3.73	4.56 ± 0.04	4.38 ± 0.05	− 23.47 ± 0.05	74 ± 11 [a]
NGC 2403	SAB(s)cd	133 ± 1	3.06	6.19 ± 0.04	6.16 ± 0.06	− 21.27 ± 0.06	68 ± 32 [a]
NGC 2715	SAB(rs)c	1323 ± 1	16.40	8.60 ± 0.04	8.59 ± 0.30	− 22.49 ± 0.30	85 ± 9 [a]
NGC 3166	SAB(rs)0/a	1183 ± 1	22.00	7.21 ± 0.02	7.17 ± 0.03	− 24.54 ± 0.03	153 ± 8 [a]
NGC 3184	SAB(rs)cd	582 ± 1	9.68	7.22 ± 0.07	7.03 ± 0.06	− 22.90 ± 0.06	43 ± 9 [a]
NGC 3344	SAB(r)bc	580 ± 1	8.28	7.44 ± 0.04	7.39 ± 0.05	− 22.20 ± 0.05	74 ± 9 [a]
M96	SAB(rs)ab	888 ± 1	10.62	6.32 ± 0.02	6.33 ± 0.04	− 23.80 ± 0.04	128 ± 4 [a]

Table 1 – *continued*

Name	Hubble type	v_h (km s^{-1})	Dist. (Mpc)	K_s (2MASS)	K_s	M_{K_s}	σ (km s^{-1})
(1)	(2)	(3)	(4)	(5)	(6)	(7)	(8)
NGC 3486	SAB(r)c	678 ± 1	12.60	8.00 ± 0.04	8.09 ± 0.04	−22.41 ± 0.04	65 ± 3 [a]
M65	SAB(rs)a	803 ± 2	14.60	6.07 ± 0.02	6.00 ± 0.04	−24.82 ± 0.04	138 ± 3 [a]
NGC 3726	SAB(r)c	864 ± 1	13.00	7.78 ± 0.05	7.61 ± 0.06	−22.96 ± 0.06	42 ± 9 [a]
NGC 4157	SAB(s)b	771 ± 1	15.10	7.36 ± 0.02	7.31 ± 0.02	−23.89 ± 0.02	90 ± 4 [a]
M98	SAB(s)ab	−142 ± 4	13.60	6.89 ± 0.02	6.83 ± 0.05	−23.83 ± 0.05	132 ± 7 [a]
NGC 4216	SAB(s)b	131 ± 4	14.10	6.52 ± 0.02	6.50 ± 0.04	−24.25 ± 0.04	197 ± 8 [a]
M106	SAB(s)bc	448 ± 3	7.27	5.46 ± 0.02	5.43 ± 0.03	−23.88 ± 0.03	148 ± 4 [a]
M61	SAB(rs)bc	1566 ± 2	12.30	6.84 ± 0.03	6.74 ± 0.04	−23.71 ± 0.04	84 ± 3 [a]
M100	SAB(s)bc	1571 ± 1	14.20	6.59 ± 0.04	6.50 ± 0.03	−24.26 ± 0.03	83 ± 3 [a]
NGC 4526	SAB(s)0	617 ± 5	16.44	6.47 ± 0.02	6.46 ± 0.02	−24.63 ± 0.02	213 ± 9 [a]
NGC 4527	SAB(s)bc	1736 ± 1	14.20	6.93 ± 0.02	6.95 ± 0.04	−23.81 ± 0.04	135 ± 8 [a]
NGC 4535	SAB(s)c	1964 ± 1	15.60	7.38 ± 0.05	8.02 ± 0.06	−23.82 ± 0.06	102 ± 10 [a]
NGC 4559	SAB(rs)cd	814 ± 1	8.91	7.58 ± 0.05	7.61 ± 0.06	−22.14 ± 0.06	49 ± 9 [a]
NGC 4569	SAB(rs)ab;Sy	−235 ± 4	17.00	6.58 ± 0.03	6.59 ± 0.05	−24.66 ± 0.05	136 ± 3 [a]
NGC 4579	SAB(rs)b;Sy	1517 ± 1	23.00	6.49 ± 0.03	6.38 ± 0.04	−25.43 ± 0.04	165 ± 4 [a]
NGC 4654	SAB(rs)cd	1036 ± 1	13.10	7.74 ± 0.03	7.75 ± 0.06	−22.83 ± 0.06	48 ± 9 [a]
NGC 5005	SAB(rs)bc;Sy	946 ± 5	14.60	6.44 ± 0.02	6.42 ± 0.04	−24.40 ± 0.04	172 ± 8 [a]
M83	SAB(s)c	513 ± 2	4.61	4.62 ± 0.02	4.57 ± 0.05	−23.75 ± 0.05	–
M101	SAB(rs)cd	241 ± 2	7.00	5.51 ± 0.05	5.43 ± 0.05	−23.80 ± 0.05	24 ± 9 [a]
NGC 5746	SAB(rs)b	1728 ± 2	34.70	6.88 ± 0.02	6.82 ± 0.04	−25.89 ± 0.04	200 ± 8 [a]
NGC 5985	SAB(r)b;Sy	2522 ± 3	61.10	8.15 ± 0.04	8.07 ± 0.06	−25.86 ± 0.06	158 ± 8 [a]
NGC 6384	SAB(r)bc	1665 ± 1	20.70	7.53 ± 0.04	7.42 ± 0.05	−24.16 ± 0.05	124 ± 7 [a]
				SB galaxies			
NGC 613	SB(rs)bc	1481 ± 5	15.40	7.03 ± 0.03	7.01 ± 0.04	−23.92 ± 0.04	126 ± 19 [b]
NGC 1097	SBb;Sy1	1271 ± 3	24.90	6.25 ± 0.03	6.23 ± 0.03	−25.75 ± 0.03	195 ± 10 [b]
NGC 1291	SB0/a	839 ± 2	9.08	5.66 ± 0.02	5.37 ± 0.02	−24.42 ± 0.02	162 ± 18 [b]
NGC 1365	SBb(s)b;Sy	1636 ± 1	17.80	6.37 ± 0.04	6.40 ± 0.04	−24.85 ± 0.04	151 ± 20 [b]
NGC 1433	SB(rs)ab;Sy2	1076 ± 1	9.04	7.06 ± 0.04	7.01 ± 0.04	−22.76 ± 0.04	113 ± 3 [b]
NGC 1672	SB(r)bc;Sy2	1331 ± 3	11.40	7.02 ± 0.03	6.94 ± 0.03	−23.35 ± 0.03	111 ± 3 [b]
NGC 2903	SB(s)d	550 ± 1	10.40	6.04 ± 0.02	5.96 ± 0.05	−24.12 ± 0.05	89 ± 4 [a]
NGC 3198	SB(rs)c	660 ± 1	14.50	7.78 ± 0.04	7.74 ± 0.06	−23.06 ± 0.06	46 ± 9 [a]
NGC 3319	SB(rs)cd	739 ± 1	13.40	10.07 ± 0.05	9.11 ± 0.06	−21.52 ± 0.06	87 ± 9 [a]
NGC 3351	SB(r)b;HII	779 ± 1	9.30	6.66 ± 0.04	6.56 ± 0.04	−23.28 ± 0.04	120 ± 9 [a]
M108	SB(s)cd	699 ± 1	8.80	7.04 ± 0.02	7.11 ± 0.02	−22.99 ± 0.02	79 ± 10 [a]
NGC 3953	SB(r)bc	1052 ± 1	15.40	7.05 ± 0.03	7.00 ± 0.05	−23.94 ± 0.05	116 ± 3 [a]
NGC 4442	SB(s)0	547 ± 5	15.30	7.29 ± 0.02	7.28 ± 0.03	−23.64 ± 0.03	187 ± 8 [a]
M91	SBb(rs);Sy	486 ± 4	17.90	7.12 ± 0.03	6.76 ± 0.04	−24.51 ± 0.04	113 ± 9 [a]
NGC 4593	SB(rs)b;Sy1	2492 ± 6	38.50	7.98 ± 0.03	7.78 ± 0.04	−25.14 ± 0.04	105 ± 5 [b]
NGC 4731	SB(s)cd	1491 ± 1	12.40	9.78 ± 0.06	9.39 ± 0.06	−21.08 ± 0.06	–
NGC 4754	SB(r)0-	1351 ± 5	15.90	7.41 ± 0.03	7.34 ± 0.03	−23.66 ± 0.03	185 ± 4 [a]
NGC 4945	SB(s)cd;Sy2	563 ± 3	3.58	4.48 ± 0.02	4.44 ± 0.05	−23.33 ± 0.05	134 ± 20 [b]
M51b	SB0;pec	465 ± 1	7.31	6.25 ± 0.03	6.34 ± 0.04	−22.98 ± 0.04	125 ± 8 [a]
NGC 5792	SB(rs)b	1926 ± 1	26.20	7.71 ± 0.03	7.66 ± 0.04	−24.44 ± 0.04	–
NGC 5850	SB(r)b	2545 ± 1	17.80	8.10 ± 0.04	7.89 ± 0.04	−23.36 ± 0.04	140 ± 7 [a]
NGC 7582	SB(s)ab;Sy2	1575 ± 7	22.30	7.32 ± 0.02	7.36 ± 0.03	−24.38 ± 0.03	113 ± 3 [b]

Notes. (1) Galaxy name. (2) Hubble type from Jarrett et al. (2003). (3) Heliocentric velocity from NED. (4) Mean of distance determinations from NED (based on primary distance indicators if available; see also Paper II for more references). (5) Total magnitude in the K_s band from 2MASS. (6) Total magnitude in the K_s band measured in this work. (7) Total absolute magnitude in the K_s band measured in this work. Magnitudes for ETGs measured in this work were derived using 2MASS image tiles (see Section 3.6). Uncertainties in our magnitudes are solely from GALFIT models. (8) Stellar velocity dispersion data from the next references: (a) Ho et al. (2009); (b) Hyperleda data base (Paturel et al. 2003).

Particularly, for the LGA a set of custom-made mosaics and additional data products were generated for more than 600 objects, classified along the Hubble type: elliptical, S0s, spirals, and barred spirals, as well as dwarf and peculiar galaxies. Galaxies range in size from 2 arcmin to 2°, with a spatial resolution [PSF full width at half-maximum (FWHM), depending on the atmospheric seeing] of ∼2–3 arcsec in the J (1.2 μm), H (1.6 μm), and K_s (2.2 μm) bands. LGA images reach a 1σ background noise at $J = 21.4$ mag arcsec^{-2}, $H = 20.6$ mag arcsec^{-2}, and $K_s = 20.0$ mag arcsec^{-2} (Jarrett et al. 2003). Therefore, LGA sample has enough sensitivity and angular resolution to allow detailed studies of galaxy structure. These images show spiral arms, bulges, bars, and star-forming regions (for more details, see Jarrett et al. 2003, and references therein). In addition, NIR observations, as mentioned in Section 1, are less affected by extinction than in the optical. Nevertheless, it was brought to our attention that LGA mosaics suffered from background oversubtraction (Jarrett 2011, private communication cited in Schombert & Smith 2012) produced by using not sufficiently large apertures around

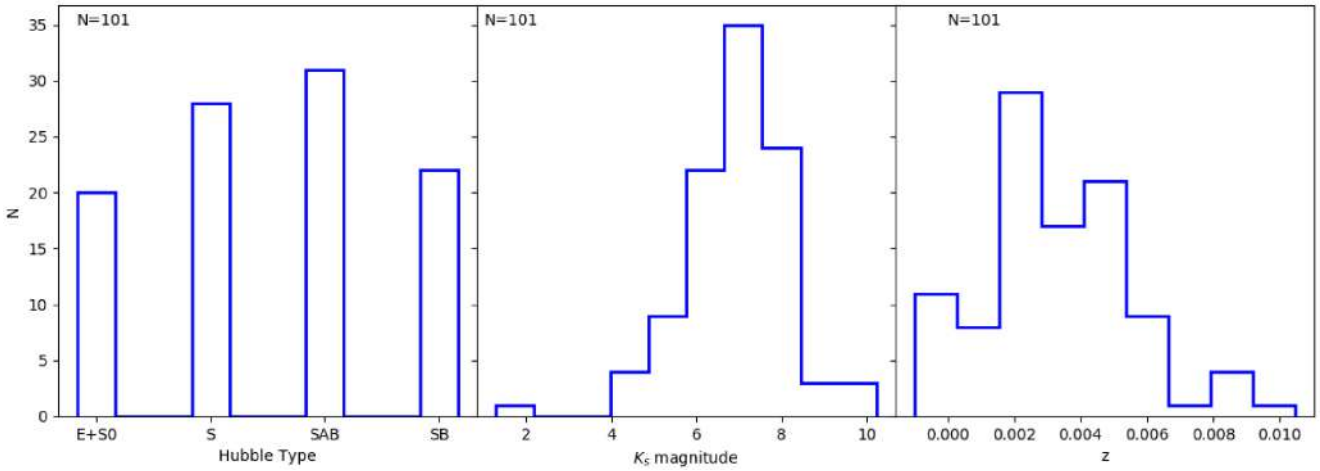

Figure 1. Sample distribution of our galaxies in Hubble type (left-hand panel), brightness in the K_s band (middle panel), and redshift (right-hand panel).

bright ETGs. This produced an underestimation of the background during the mosaic generation.[3] As expected, a deficit in the total magnitudes of ETGs was found (e.g. Schombert & Smith 2012), causing inaccuracies in other related parameters, such as effective radii. The resulting background oversubtraction error on the LGA mosaics has some affinity with the one reported by Lauer et al. (2007) for SDSS photometry data on ETGs, which was corrected in the later SDSS data releases (e.g. Blanton et al. 2011, for DR8). Below (see Section 3.6), we present a detailed analysis using LGA mosaics and 2MASS image tiles downloaded from the NASA/IPAC Infrared Science Archive (IRSA).[4]

According to their 2MASS K_s-band integrated fluxes and distances (see Fig. 1), galaxies in Table 1 are among the brightest nearby quiescent galaxies (columns 4–7 in Table 1). We have directed our selection to cover the distribution of morphological types, from early- to late-type systems, such as ellipticals, lenticulars, and intermediate and barred spirals (column 2 in Table 1); besides, by covering most of Hubble types and especially disc galaxies, we are able to examine internal structures over a wide range of luminosities and sizes, allowing the exploration of classical bulges and pseudo-bulges distribution.

2.2 Velocity dispersion data

Stellar velocity dispersion data (column 8 in Table 1) were taken from the literature, mainly from the work of Ho et al. (2009) and Hyperleda data base[5] (Paturel et al. 2003).

3 METHODOLOGY

3.1 2D decomposition with GALFIT

We used the GALFIT[6] (Peng et al. 2002, 2010) algorithm to extract the structural parameters of the galaxies, such as total magnitudes, effective radii, and concentration indices, among others, from the surface brightness distribution modelling. GALFIT performs a photometric 2D decomposition on digital images of galaxies, stars, or other astronomical sources. The modelling is carried out through parametric functions, such as Sérsic, Exponential, Nuker, Gaussian, Moffat, and Ferrer, among others, and it can also be used to perform multiple fits on several objects simultaneously. Some wrapper scripts have been implemented to fit galaxies in crowded regions, such as in clusters of galaxies (e.g. Añorve 2012; Barden et al. 2012).

GALFIT uses a least-squares Levenberg–Marquardt minimization, while the goodness of the fit is computed by the chi-square, χ^2 statistics, then calculates the parameters for the next step and continues iterating until the χ^2 is minimized. The indicator of the goodness of the fit is the reduced χ^2, χ^2_ν:

$$\chi^2_\nu = \frac{1}{N_{\rm dof}} \sum_{x=1}^{nx} \sum_{y=1}^{ny} \frac{\left[f_{\rm img}(x,\,y) - f_{\rm mod}(x,\,y)\right]^2}{\sigma(x,\,y)^2}, \quad (1)$$

where $N_{\rm dof}$ is the number of degrees of freedom in the fit; nx and ny are the image dimensions; $f_{\rm img}(x,\,y)$ is the value of the $(x,\,y)$ pixel of the galaxy image; $f_{\rm mod}(x,\,y)$ is the value of the corresponding pixel of the PSF-convolved model image generated at each iteration; and $\sigma(x,\,y)$ is the 'sigma' image, which is the error on each pixel and is generated internally by GALFIT.

GALFIT reads the image header to access the exposure time and *GAIN*, while the magnitude zero-point is taken from the input parameters file. The image ADUs are converted into electrons using the *GAIN* parameter, so that $ADU \times GAIN = electrons$. The magnitude zero-point is used to convert pixel counts and fluxes into a physical magnitude. The PSF is provided by the user. A good PSF is generated by using bright, isolated non-saturated stars. GALFIT convolves the PSF image with the model during the fit to account for the effects of seeing and/or also to fit a PSF as a model component. The PSF image is obtained using the SExtractor (Bertin & Arnouts 1996) 'objects' image to select the star among the potential candidates. We also have excluded bad pixels or objects from the fit by manually masking them (in most of the images of our sample, the bright stars were already masked), using the SExtractor 'segmentation' image, which is modified when such pixels or objects are selected in order to set all the non-zero valued pixels that will be ignored during the fit (see Peng et al. 2010, for further details). Parameters are allowed to vary during the fit.

[3]See the discussion by Tom Jarret in https://wise2.ipac.caltech.edu/staff/jarrett/2mass/ellipticals.html.
[4]2MASS image tile service (https://irsa.ipac.caltech.edu/applications/2MASS/IM/interactive.html#pos).
[5]Data available at http://leda.univ-lyon1.fr/leda/param/vdis.html.
[6]Software available at https://users.obs.carnegiescience.edu/peng/work/galfit/galfit.html.

Initial parameters are generated by SExtractor and then are parsed to GALFIT, namely the centroid x and y pixel positions, initial total magnitude, initial axial ratio, and effective radius. The Sérsic index is initially set to $n \sim 2$, depending on the morphological type of the galaxy.

3.2 Model selection

Based on the morphological type reported by 2MASS (Jarrett et al. 2003) and listed in column 4 of Table 1, we considered mainly three models when adjusting the surface brightness of galaxies: usually a single component represented by a Sérsic profile for elliptical galaxies; bulge and disc components of lenticular and spiral galaxies are modelled by Sérsic and exponential functions, respectively; however, bulge, disc, and bar components are considered for barred galaxies, where bars are modelled also by a Sérsic profile. For those sources classified as AGN, their models can include an additional PSF component to fit the unresolved nuclear component associated with the AGN contribution. A comprehensive discussion on the applicability of different models is given by Graham (2013).

GALFIT parametrizes the surface brightness distribution of galaxies and compact sources using axially symmetric profiles, whose radial distribution is expressed by generalized ellipses (Athanassoula et al. 1990):

$$r = \left(|x|^{(c+2)} + \left| \frac{y}{q} \right|^{(c+2)} \right)^{\frac{1}{(c+2)}}, \quad (2)$$

where q is the ratio of the major axis to the minor axis, while c indicates the boxiness/disciness of the ellipses.

The popularity of the Sérsic profile (Sérsic 1963, 1968) has grown since its revival during the 90's (e.g. Caon, Capaccioli & D'Onofrio 1993). It has been implemented in GALFIT by the following expression:

$$I(r) = I_{\rm e} \exp\left[-\kappa \left(\left(\frac{r}{r_{\rm e}} \right)^{1/n} - 1 \right) \right], \quad (3)$$

where $I(r)$ is the surface brightness at the radius r and κ is a parameter coupled to the Sérsic index n, a measure of the concentration of the light profile, in such way that $I_{\rm e}$ is the surface brightness at the effective radius $r_{\rm e}$ (radius where half of the total flux is within it). When $n = 4$, then $\kappa = 7.669\ 25$ and we have the de Vaucouleurs (1948) profile.

The exponential profile (Freeman 1970) is also a special case of the Sérsic function when $n = 1$. It is given by the following expression:

$$I(r) = I_0 \exp\left(-\frac{r}{r_{\rm s}} \right), \quad (4)$$

where I_0 is the central surface brightness and $r_{\rm s}$ is the scale length of the disc. $r_{\rm s}$ is related to the effective radius $r_{\rm e}$ by $r_{\rm e} = 1.678 r_{\rm s}$.

To model the bar component, as mentioned above, we used a Sérsic profile with $n \leq 0.5$, which is often used in literature for this purpose (e.g. Greene, Ho & Barth 2008; Peng et al. 2010).

Fits to the surface brightness distribution of galaxies were done following the steps described below:

(i) SExtractor was used to generate input parameters. Then, we first modelled with Sérsic profile, regardless of the galaxy morphology.

(ii) Elliptical galaxies are expected to be well described by a Sérsic profile, but we do not discard fitting an additional component (double Sérsic or exponential profile), to respond to the possible existence of substructures that resemble extended stellar envelopes or embedded discs (e.g. Läsker, Ferrarese & van de Ven 2014). Hence, some ellipticals in our sample have been fitted with an additional component to the Sérsic component described above and, when it is the case, we also call bulge to that central component having a higher n (also a checking on q ratio and morphology of the additional substructure is done).

(iii) For disc galaxies, lenticulars, and normal spirals, an additional run is made with a single-exponential disc component.

(iv) For barred spiral galaxies, we proceeded in the same way, adding a third component to fit the bar. In the case of intermediate spirals (SAB), some of them are well fitted with two components, others may need three components, while in some cases the models between an SAB galaxy with two and three components are quite similar.

(v) The sky background component is also considered as a free parameter in the GALFIT runs.

(vi) We include all the components considered previously (for instance, Sérsic, disc, and/or bar models depending on the morphological type of the galaxy), using their outputs as initial parameters, to run a simultaneous fit to arrive at the final model.

(vii) The selection of the best-fitting model is based on the goodness of the fit (reduced χ^2) and through a visual inspection of residual image. We improved our models by including additional components to account for symmetrical structures identified in the residual images (generally bars or an extra component for some ellipticals).

3.3 Uncertainties

The uncertainties of parameters returned by GALFIT underestimate the true error bars, which are typically ∼0.01 mag and ∼0.05 arcsec for $r_{\rm e}$ (e.g. Häussler et al. 2007). Therefore, we have used a different approach to derive more realistic uncertainties. We refer the reader to Appendix A for a detailed description and discussion on the procedure for estimating the final uncertainties, reported in this paper.

3.4 Surface brightness profiles

We used EllipSect[7] (Añorve 2020) to generate the surface brightness profiles of galaxies from GALFIT's outputs. Besides, EllipSect is able to extract and compute the absolute magnitude, luminosity, flux, total apparent magnitude, Akaike information criterion (AIC), and Bayesian information criterion (BIC), among other parameters. 1D profiles are useful to evaluate the choice of the final model generated through the 2D decomposition, since the need of additional components may be noticed when comparing the surface brightness profiles of the galaxy and its model.

Examples of the photometric decomposition carried out with GALFIT are shown in Fig. 2 along with the 1D profiles generated using EllipSect for the galaxies NGC 4125, M51a, and M91.

3.5 Extinction and *k*-correction

The NIR magnitudes were corrected for Galactic extinction according to Schlegel, Finkbeiner & Davis (1998), as provided by the NASA/IPAC Infrared Science Archive.[8]

[7] Software available at http://github.com/canorve/EllipSect.
[8] https://irsa.ipac.caltech.edu/applications/DUST/

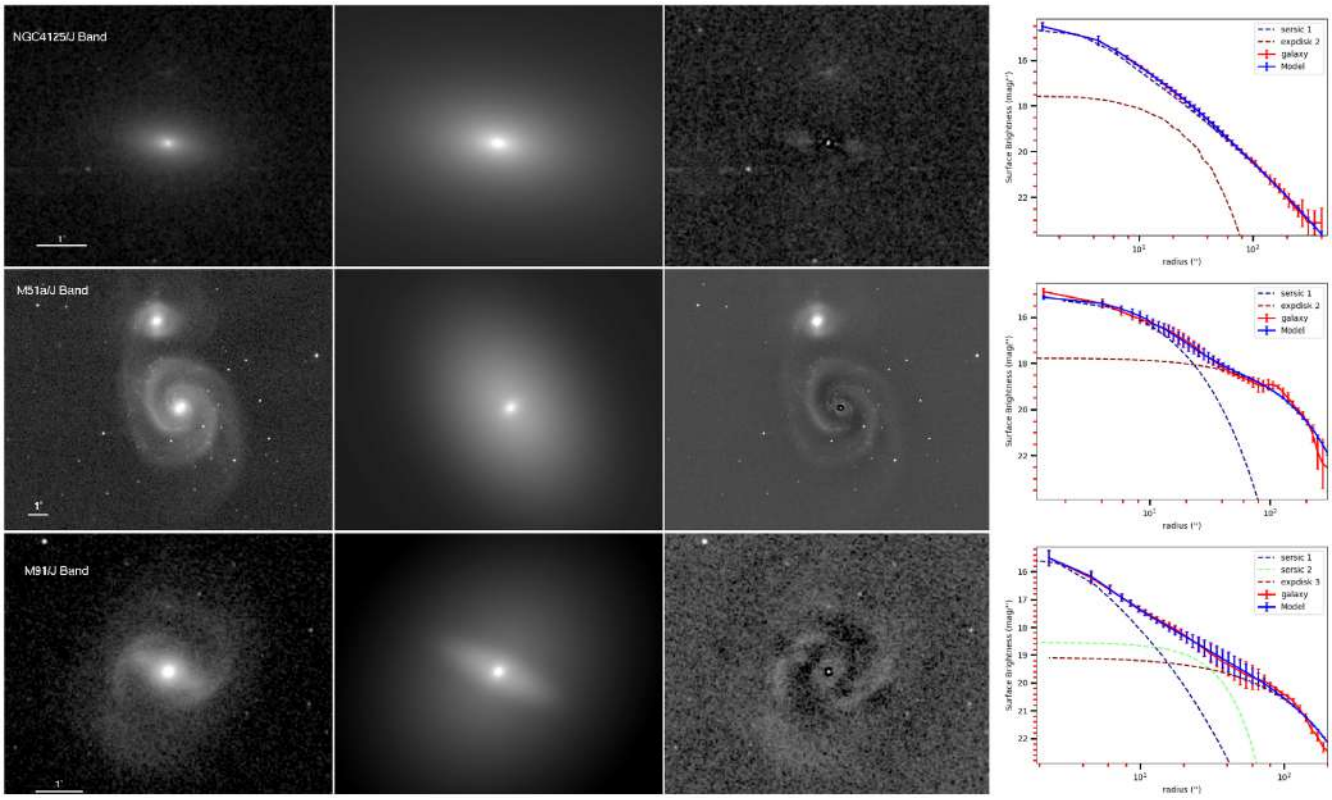

Figure 2. Examples of GALFIT decomposition method for the galaxies NGC 4125, M51a, and M91 from top to bottom, respectively. The images are, from left to right: 2MASS image, model, and residual images generated with GALFIT and 1D surface brightness profile generated with EllipSect.

Additionally, we applied *k*-corrections to the magnitudes using the galaxy's redshift and the $J - K_s$ and $H - K_s$ colours, according to the prescription from Chilingarian, Melchior & Zolotukhin (2010), which is also available online.[9] The Chilingarian et al. (2010) scheme to generate *k*-correction is comparable to the one developed by Mannucci et al. (2001).

3.6 Issues with the LGA photometry

We have performed a comparison between data from the 2MASS by using data from the LGA mosaics and IRSA image tiles. We found disagreement among the structural parameters and the integrated total magnitudes for ETGs. The discrepancy was produced by the sky subtraction during the LGA mosaic generation. We show in Fig. 3 the surface brightness profiles of the ETGs NGC 3115 and NGC 1947 and the LTG M61. It can be seen how the surface brightness profiles of ETGs, generated on LGA mosaics (red line), show a steep drop-down than the surface brightness generated on IRSA image tiles (blue line); however, for the LTG M61, the results are indistinguishable using either the LGA mosaic or the image tile. The LGA mosaics were made available to us by Jarret (2012, private communication) in a manageable set, where bright objects around the target galaxy were masked. We initially worked with the 101 galaxies in our sample using the LGA mosaics.

We repeated our analysis for all the 20 ETGs (E+S0) in our sample using the IRSA image tiles, where bright objects were masked. Fig. 4 shows the comparison between the total magnitudes of ETGs using both data sets. The total magnitudes measured on IRSA tiles are brighter, according the following offsets:

Band	Offset
J	0.32 ± 0.08 mag
H	0.34 ± 0.06 mag
K_s	0.34 ± 0.07 mag

These results are consistent with the ∼0.33 mag offset reported by Schombert (2011) and Schombert & Smith (2012), and the mean 0.34 mag offset found in the much deeper photometric K_s study by Läsker et al. (2014). Besides, for the few galaxies that we have in common with Schombert & Smith (2012), our measurements for their reported J and K_s magnitudes (red points in Fig. 4) are in agreement. As expected, an offset of 0.20 dex in the effective radius (r_e) of the galaxy was found for elliptical galaxies between data from the LGA mosaics and IRSA image tiles. These offsets are shown in Fig. 5 for the J, H, and K_s bands. Our results are consistent with Cappellari et al. (2011), who found a larger offset.

We should note that Schombert and Smith generated image cut-outs from the 2MASS survey images using their own scripts. Besides, the sky determinations were generated by a slightly different approach to ours, and the surface brightness measurements were done using a 1D technique. Nevertheless, despite all those differences, our reported total magnitudes and offsets are in close agreement with Schombert & Smith (2012).

A correction for ETGs photometry using LGA mosaics can be generated from the offsets found above, at the risk of sacrificing

[9] http://kcor.sai.msu.ru

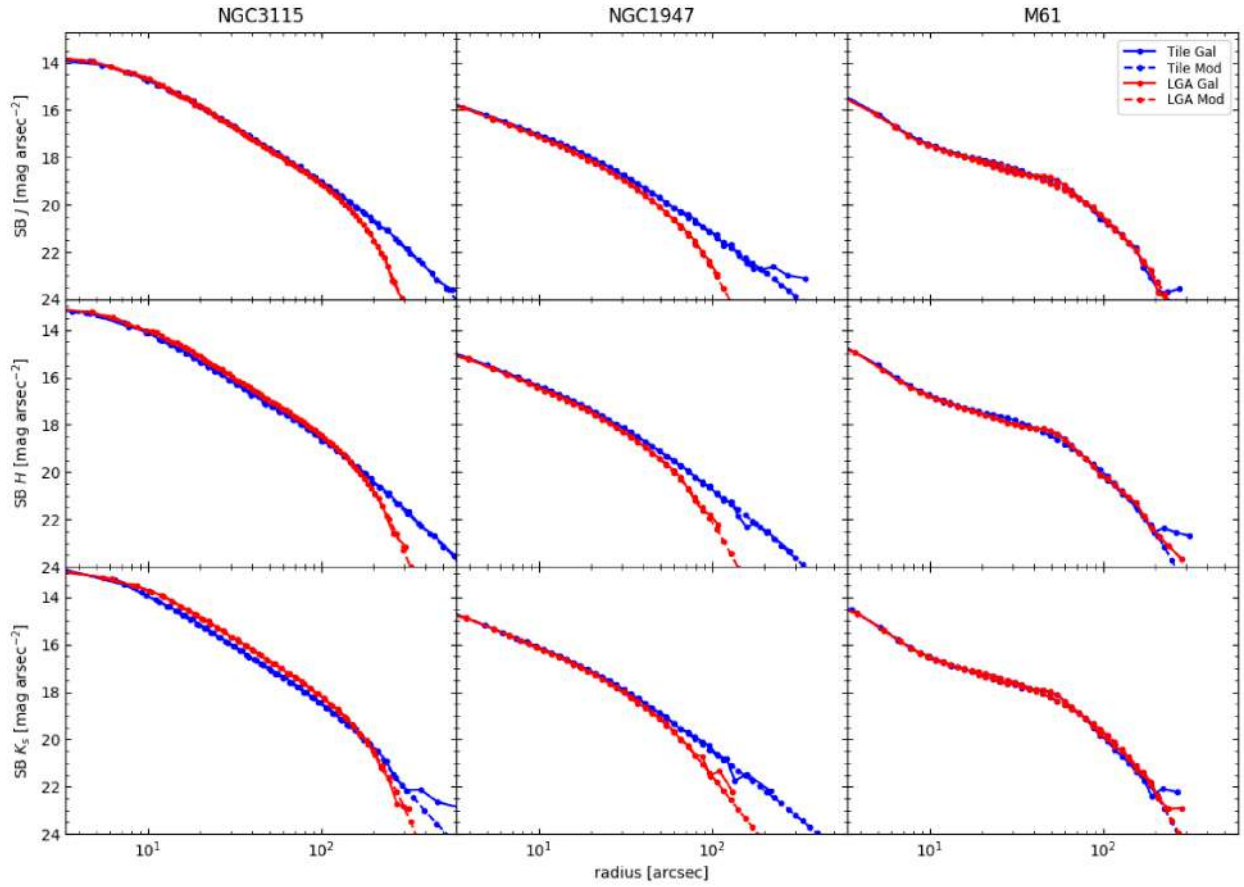

Figure 3. Surface brightness profiles using LGA mosaics (red points and lines) and IRSA image tiles (blue points and lines) for the 2MASS data, for the ETGs NGC 3115 (left) and NGC 1947 (centre), and the LTG M61 (right). Solid lines represent the galaxy profile, while dashed lines are for the models generated with GALFIT. From top to bottom panel are shown the J, H, and K_s bands, respectively. An abrupt drop down is seen in the profiles for ETGs using LGA mosaics, while for the LTG the profiles are consistent using either LGA mosaics or 2MASS IRSA image tiles.

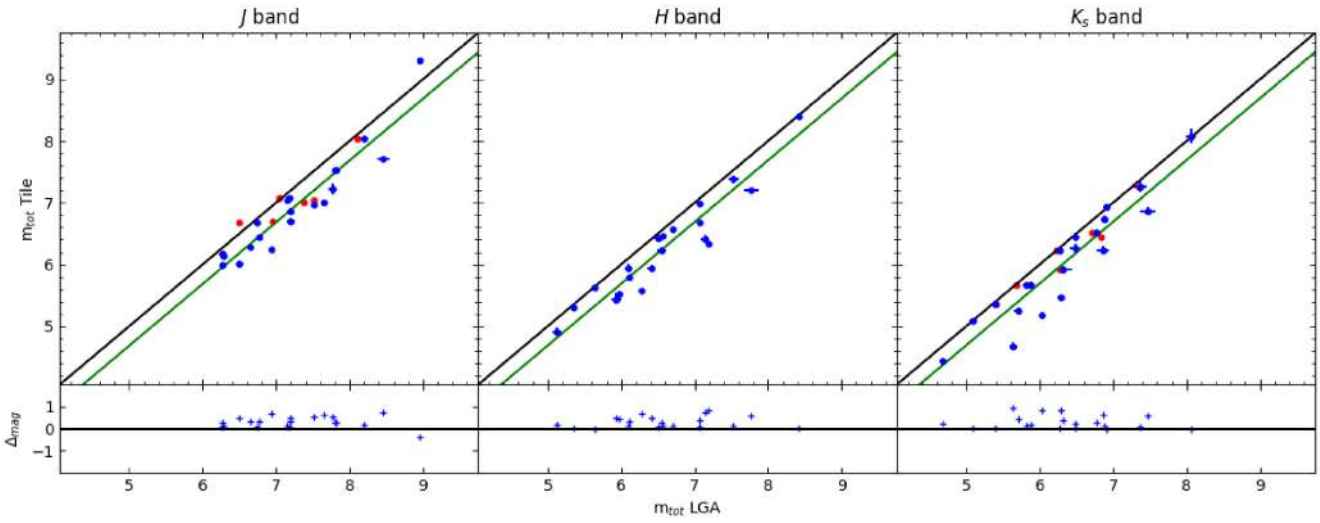

Figure 4. Comparison between total magnitudes for ETGs in our sample using the 2MASS data for LGA mosaics and image tiles in the J, H, and K_s bands. Black lines represent the one-to-one correspondence, while the green ones represent an offset of ∼0.35 mag per band. Red points are galaxies in common with Schombert (2011).

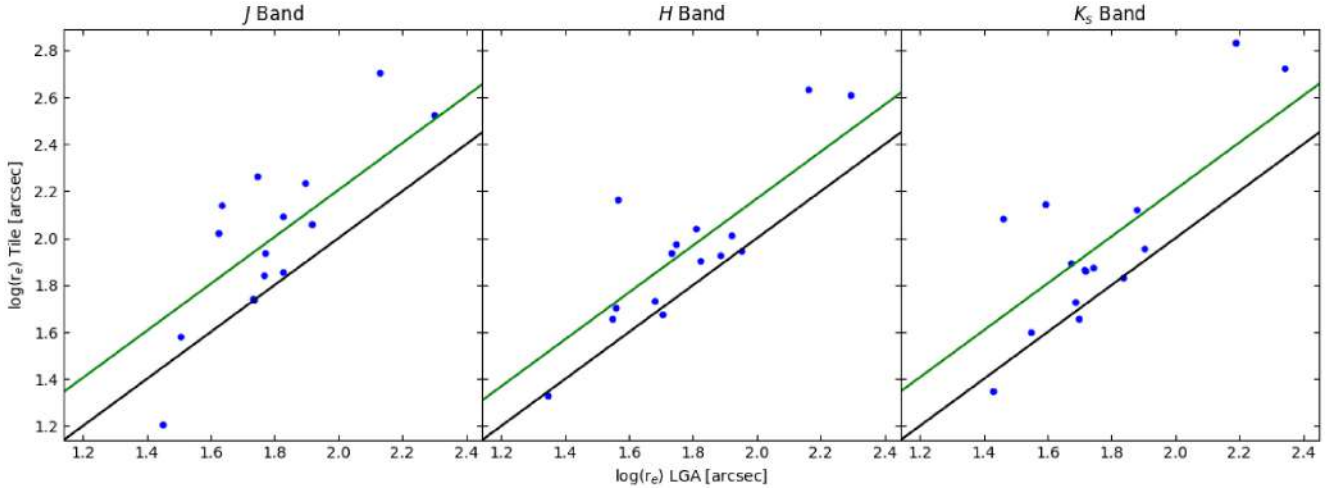

Figure 5. Same as previous image, but for effective radii of galaxies estimated using LGA mosaics and IRSA image tiles for E galaxies in our sample. Black lines represent the one-to-one correspondence, while the green ones represent an offset of ∼0.20 dex per band.

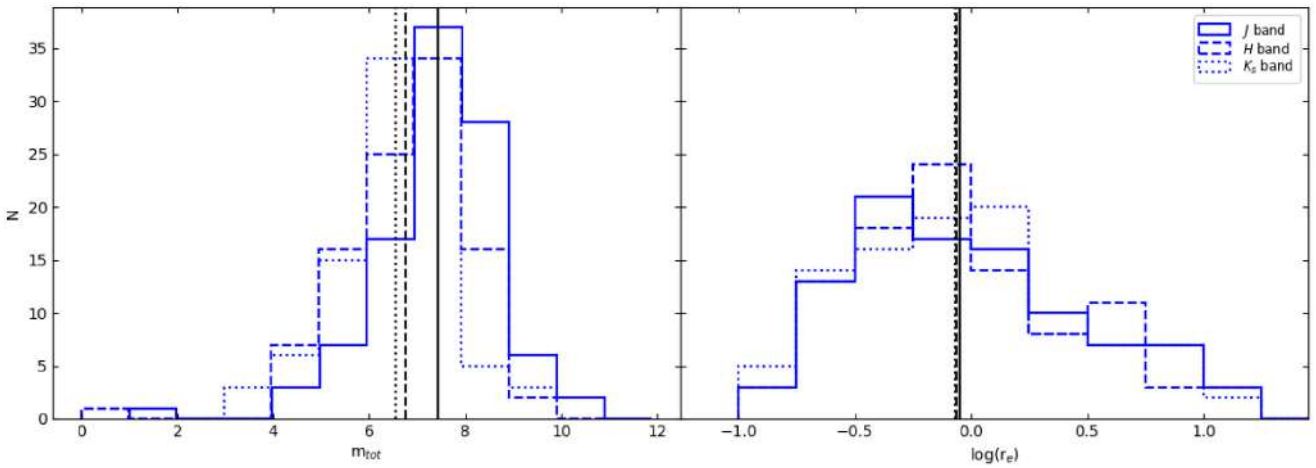

Figure 6. Distribution magnitudes (left-hand panel) and effective radii obtained from our photometric analysis. Solid line is for the *J* band, while dashed and dotted lines are for the *H* and K_s bands, respectively. In the same way, vertical lines indicate the mean of each distribution.

precision. Therefore, for the rest of the paper we report the photometric analysis for the 20 ETGs in our sample, generated on images from the IRSA tile server. On the other hand, since the results for LTG photometry using LGA mosaics are indistinguishable from those derived using IRSA tiles, hereafter, we report the photometric analysis for the 81 LTGs in our sample generated from LGA mosaics.

As a conclusion, we recommend, when dealing with bright ETGs, to avoid using 2MASS LGA mosaics or the reported measurements based on them. For example, some of the K_s total magnitudes adopted by the MASSIVE Survey (Ma et al. 2014, their table 3) might be underestimated, as indicated in this paper.

4 RESULTS

4.1 Photometry and structural properties

In this section, we report the results of our 2D surface brightness modelling with GALFIT, including the structural parameters such as magnitudes for each component (Table 3), as well as effective radii, Sérsic indices (*n*), ellipticities, and position angles (Tables 4, 5, and 6 for each band of 2MASS). These tables (from 3 to 6) are presented only in digital format. In such tables, subscripts 1, 2, and 3 for parameters refer to bulge component (or the single component in the case of some E galaxies), disc or envelope (see below Section 4.1.1), and bar, respectively. The r_s value reported in digital tables for E galaxies with an additional Sérsic component refers to their r_e.

As it can be seen below in Fig. 6, our results look quite similar in the three 2MASS bands, where the distributions of total magnitudes and effective radii are displayed. Thereby, this allows us to have a better control of the structural parameters modelled with GALFIT, since quite similar conclusions are reached regardless of the NIR band used.

4.1.1 Two-component fits to elliptical galaxies

Some elliptical galaxies were modelled using two Sérsic components (e.g. Capaccioli 1989, for a view on early attempts). Thus, when talking about bulge parameters for the complete sample, we refer to the central component that has the highest Sérsic index.

In order to carry out a more robust selection of the final model for these E galaxies, we applied the AIC (Akaike 1974) and BIC (Schwarz 1978) implemented in EllipSect. AIC and BIC are based on the χ^2 statistics and the numbers of parameters used in the model

to penalize the overfitting of parameters added to the model. Then, the model with the lowest AIC and BIC values is the selected.

Below, we show the n values for the E galaxies with two components in the J band (also in the H and K_s bands is performed the same methodology for such E galaxies) using IRSA image tiles (see Section 3.6); full results are disclosed in Tables 3–6. Therefore, M32 (cE2) was modelled with a bulge component with $n = 4.25$ plus a disc component. M87 (E+0-1) has $n = 1.27$ for the central component, while the additional component, the extended stellar envelope, has $n = 0.99$. The surface brightness model of M60 (E2) has a bulge component with $n = 2.09$, while the extra component is also a Sérsic with $n = 1.47$. M105 (E1) was best fitted with a Sérsic component with $n = 3.21$ plus a disc exponential profile as an additional component. The surface brightness distribution of M110 (E5) was modelled with a double Sérsic component, with $n = 2.51$ and 0.97 for the bulge and the extended envelope, respectively. In the case of NGC 1549 (E0-1), a Sérsic component with $n = 6.31$ was fitted along with a disc exponential profile. The model of NGC 3377 (E5-6) has two Sérsic components, with n values of 6.55 and 2.69 for the bulge and extended envelope, respectively. NGC 4125 (E6) was fitted with Sérsic component with $n = 7.03$, plus an exponential disc profile representing an embedded disc. The central component of NGC 4697 (E6) has $n = 4.51$, while the envelope has $n = 3.01$. Finally, the surface brightness profile of NGC 4976 (E4) was fitted with a double Sérsic with $n = 8.47$ and 1.81 for the bulge and stellar envelope, respectively.

A recent study by Huang et al. (2013a) has suggested the presence of three components in the surface brightness modelling of ETGs in the optical band V: inner, intermediate, and extended, respectively. Although the galaxies in our sample are close enough ($z \leq 0.01$) to allow enough angular resolution to recover the inner components introduced by Huang et al. (2013a), we have failed to recover those minor inner components ($r_e \sim 1$ kpc), which account for just 0.1–0.15 of the total luminosity of the galaxy. Those inner and intermediate components might be related to the continuous star formation seen in recently quenched and blue-star-forming E galaxies (Lacerna et al. 2020). Therefore, because the NIR bands used in this study trace older stellar populations, preferentially, we are unable to recover the supposedly younger inner components. More detailed comparisons between optical and NIR observations are needed to test the Integral Field Unit (IFU) analysis of Lacerna et al. (2020) or the scenario proposed by Huang et al. (2013b).

4.1.2 *Comparison with previous works*

Similarly to the comparisons of magnitudes presented above with Schombert & Smith (2012), we also compared with the results from de Jong & van der Kruit (1994) and Tully et al. (1996) for spiral galaxies in common observed in the K' band. While de Jong & van der Kruit (1994) reported photometric errors (marked below with an asterisk), Tully et al. (1996) did not. Below are shown the magnitudes for these galaxies in common:

Galaxy	m_{Ks}	m_K
M100	6.50 ± 0.03	6.47 ± 0.23 (∗)
NGC 3726	7.61 ± 0.06	7.96
NGC 3877	7.68 ± 0.05	7.75
NGC 3938	7.79 ± 0.06	7.84
NGC 3953	7.00 ± 0.05	7.03
NGC 4013	7.58 ± 0.04	7.68
NGC 4157	7.31 ± 0.02	7.52

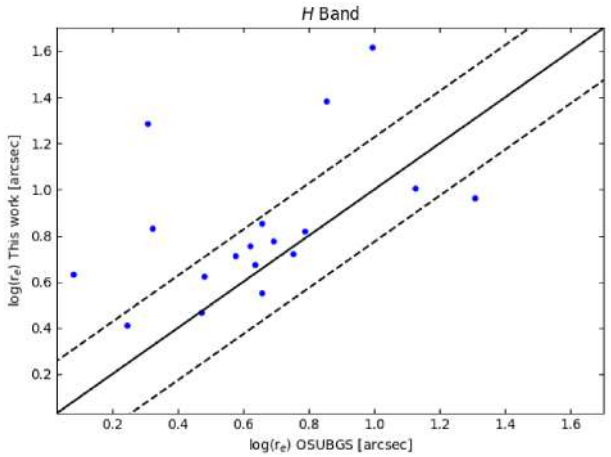

Figure 7. Comparisons between effective radii of bulges estimated in this work with those ones from Laurikainen et al. (2004a) using data from OSUBSGS in the H band. Dashed lines represent the 1σ scatter.

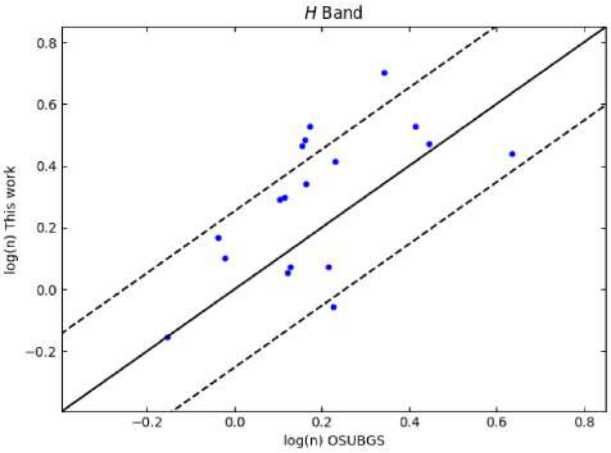

Figure 8. Same as previous image, but for Sersic index of bulges estimated in this work and those ones from Laurikainen et al. (2004a).

Despite slight differences between the 2MASS K_s and K bands used in those previous studies, our measurements are in close agreement with de Jong & van der Kruit (1994) and Tully et al. (1996). As a further matter, if the errors reported by de Jong & van der Kruit (1994) are representative for early works, then the agreement arrived in this work with the studies of de Jong & van der Kruit (1994) and Tully et al. (1996) might be called remarkable.

We have also compared our results (Figs 7 and 8) with those from the Ohio State University Bright Spiral Galaxy Survey (OSUBSGS; Eskridge et al. 2002) for the bulge parameters of effective radius and Sérsic index in the H band reported by Laurikainen et al. (2004a). We are in agreement within 1σ with the parameters reported by OSUBSGS.

4.2 Bulge/pseudo-bulge classification

We implemented a bulge/pseudo-bulge classification using the following indicators:

(i) FP correlations are used for separating classical bulges from pseudo-bulges (e.g. Kormendy & Ho 2013). Hence, we adopted the Kormendy relation (KR; Kormendy 1977), a projection of the FP, as a tool to achieve this goal. Then, it is expected that classical bulges

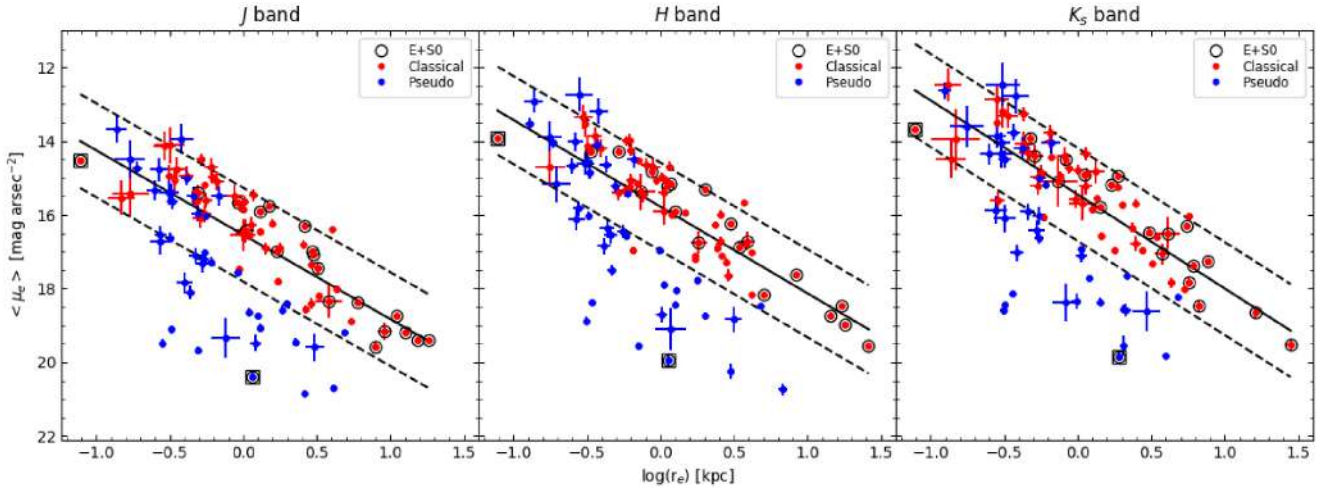

Figure 9. KR for E+S0 galaxies and bulges in our sample. Red filled circles represent classical bulges, while the blue ones are pseudo-bulges according to our final classification. Black dashed lines represent 3σ to the fit of E+S0 galaxies in our sample. The three bands of 2MASS are shown. Objects in black circle represent the E+S0 galaxies in our sample. M32 and M110 are highlighted in black squares (see Section 5.1).

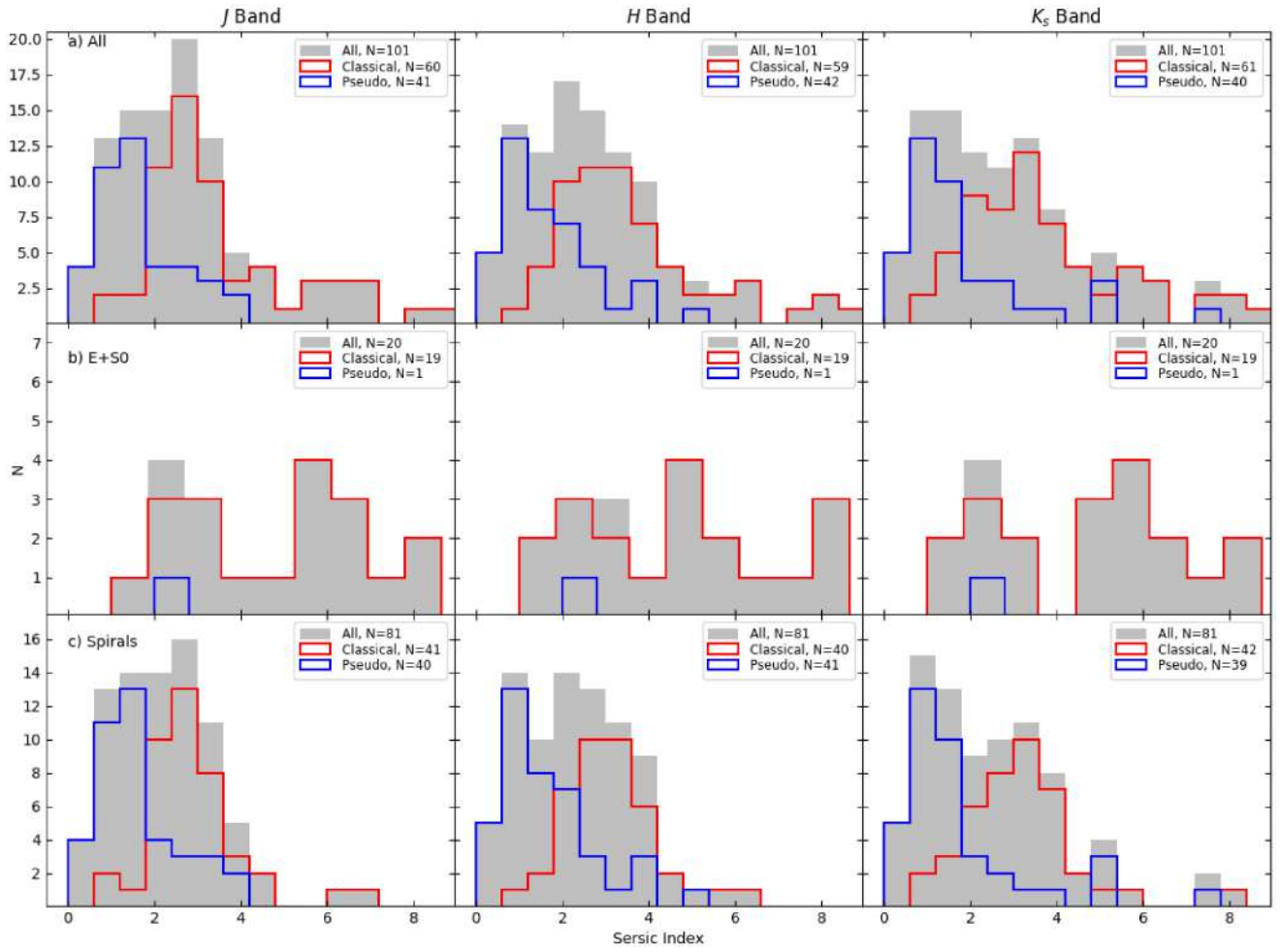

Figure 10. Distribution of the Sérsic index according to the (sub)sample of galaxies considered. Panels are from top to bottom: a) All sample, b) E+S0 galaxies, and c) spiral galaxies (S, SAB, and SB types), respectively. From left to right: J, H, and K_s bands, respectively. In all cases, grey histograms indicate the total (sub)sample, while the red and blue ones are for classical and pseudo-bulges, respectively.

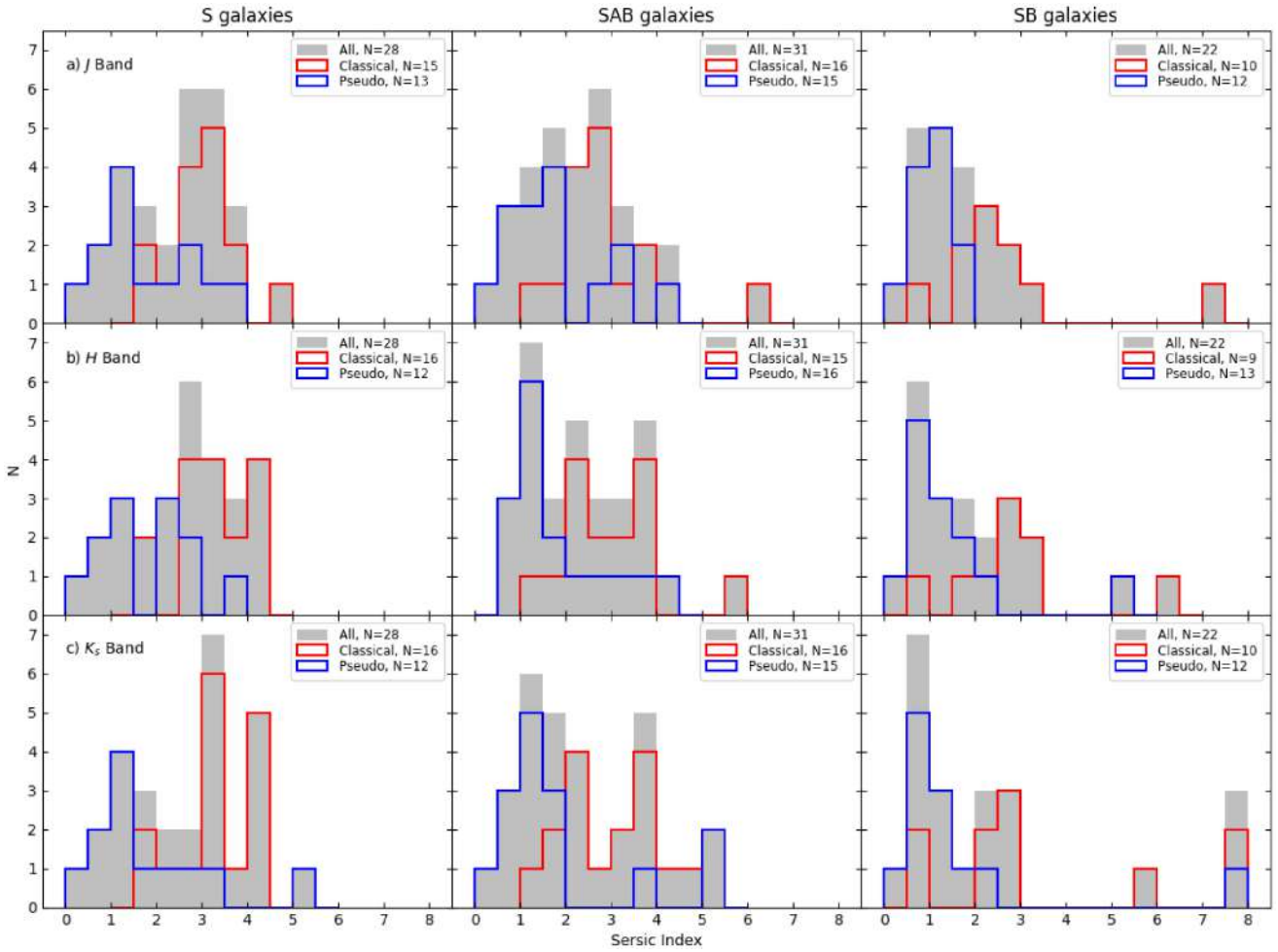

Figure 11. Distribution of the Sérsic index for spiral galaxies. Panels are from top to bottom: a) J, b) H, and c) K_s bands, respectively. From left to right: S, SAB, and SB Hubble types, respectively. Colours for histograms are the same as in Fig. 10.

follow the KR, while pseudo-bulges are expected to fall as outliers of the relation (e.g. Gadotti 2009; Añorve 2012).

(ii) Pseudo-bulges, formed from secular processes, tend to have a rotational component and a low Sérsic index $n < 2$, while classical bulges have $n \geq 2$ (Fisher & Drory 2008).

(iii) Classical bulges have high velocity dispersions, $\sigma \sim 160\,\mathrm{km\,s^{-1}}$ (Fisher & Drory 2016); however, pseudo-bulges usually have $\sigma \sim 90\,\mathrm{km\,s^{-1}}$. Since the number of pseudo-bulges with $\sigma > 130\,\mathrm{km\,s^{-1}}$ is low, we will call classical bulges those with $\sigma > 130\,\mathrm{km\,s^{-1}}$.

Therefore, *classical bulges must hold at least two of three indicators listed above*. It is worth mentioning that all of the galaxies' bulges (including those from E+S0 galaxies) have been classified. Therefore, we have that ∼60 per cent of the bulges in our sample are classical bulges, which is consistent in the three NIR bands.

4.2.1 Kormendy relation

ETGs and some bulges display a link between the effective radius, r_e, and the surface brightness at the effective radius, μ_e, known as the KR (Kormendy 1977), which implies that at r_e, larger systems are fainter than the smaller ones; thus, larger galaxies have lower densities. We have used distances of our sample to convert effective radii in physical units (as well as to compute luminosities for some scaling laws presented in the companion paper). When we applied the KR as a tool to isolate classical bulges from pseudo-bulges, the latter ones will be those objects falling 3σ out of the relation as outliers (see Fig. 9). From this analysis, we obtained that 71 per cent of the bulges are classical in the J band, while 70 per cent and 72 per cent are in the H and K_s bands, respectively.

Fig. 9 shows the KR for the elliptical galaxies and bulges of our sample in the three bands of 2MASS, making a distinction among the sources classified as classical and pseudo-bulges according to our scheme outlined above. E+S0 galaxies are closed in black circles, as well as dwarf ellipticals M110 and M32 that are also highlighted in black squares (see Section 5.1). The linear fits in KR for each band (black line) were generated considering only E+S0 galaxies.

The linear fits to the KR for each band are given by the following expressions:

$$\begin{cases} \mu_e(J) = (2.29 \pm 0.29)\log r_e(J) + 16.54 \pm 0.33 : & J \text{ band}, \\ \mu_e(H) = (2.35 \pm 0.24)\log r_e(H) + 15.78 \pm 0.30 : & H \text{ band}, \\ \mu_e(K_s) = (2.55 \pm 0.27)\log r_e(K_s) + 15.45 \pm 0.28 : & K_s \text{ band}. \end{cases}$$

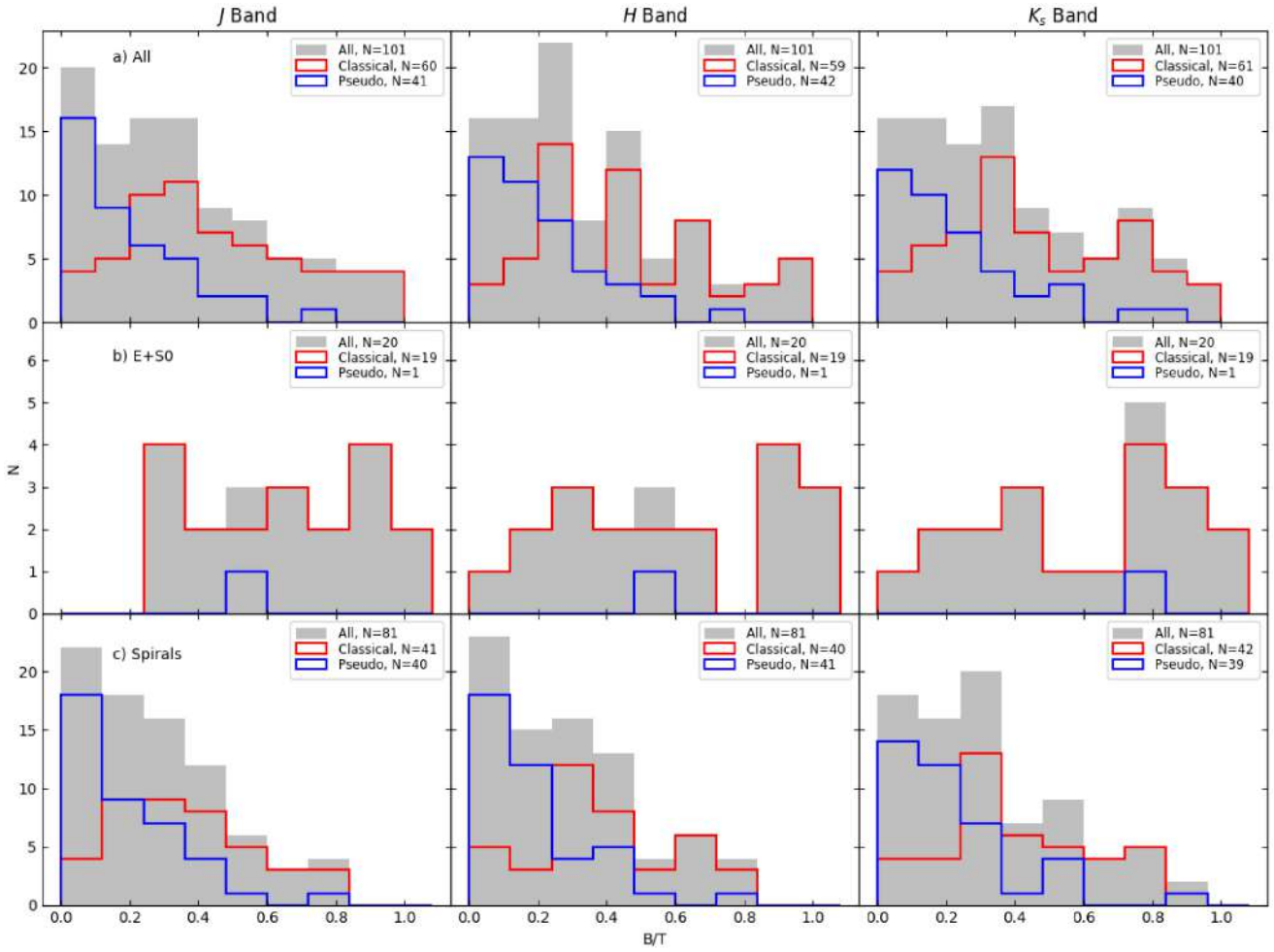

Figure 12. Distribution of the *B*/*T* ratio according to the (sub)sample of galaxies considered. Panels are from top to bottom: a) All sample, b) E+S0 galaxies, and c) spiral galaxies (S, SAB, and SB types), respectively. From left to right: *J*, *H*, and K_s bands, respectively. Colours for histograms are the same as in Fig. 10.

4.2.2 Sérsic index and velocity dispersion

Based on the Sérsic index criterion, we found that 60 per cent, 65 per cent, and 61 per cent of the bulges are classical bulges; i.e. they have $n \geq 2$ in three NIR bands employed in this study.

Using the velocity dispersion alone as a classifier, we find that 51 per cent of the 97 objects with velocity data in our sample have $\sigma \geq 130$ km s^{-1}.

4.2.3 Final classical bulge/pseudo-bulge classifications

Thus, using the criteria established earlier, we have that 41 per cent (*J*), 42 per cent (*H*), and 40 per cent (K_s) out of 101 galaxies in our sample are pseudo-bulges. The last column of Table 3, which is presented in digital format, contains the assigned bulge classification for each galaxy.

4.3 Sérsic index, bulge-to-total and axial ratios

The distributions of Sérsic index, *n*, are shown in Figs 10 and 11. While, the distributions of bulge-to-total ratio, *B*/*T*, are shown in Figs 12 and 13. These distributions are presented according to Hubble types and (sub)samples considered, such as the whole sample, E+S0, and spiral subsamples shown in panels *a*, *b*, and *c* of Figs 10 and 12, respectively, for the 2MASS bands; meanwhile, distributions for S, SAB, and SB subsamples are shown in Figs 11 and 13 for the *J*, *H*, and K_s bands in *a*, *b*, and *c* panels, respectively. We also place these results in the context of bulge types. Also, the average values of *n* and *B*/*T* for these distributions are listed in Table 2. Besides, in Fig. 14 we show the Sérsic index as a function of *B*/*T* ratio according to bulge types, where the criterion for *n* used to classified bulges is also highlighted (dashed horizontal line). From these plots, the distinction between pseudo-bulges and classical bulges becomes more evident.

Furthermore, in Fig. 15 we present the axial ratio, *q*, distribution for the whole sample with the aim of looking for additional indicators on the morphology of bulge types. We will discuss later these findings that are consistent with earlier works.

5 DISCUSSION

The 1D analysis presented by Schombert (2011) and Schombert & Smith (2012) reported that the total magnitudes of ETGs in the 2MASS XSC (Jarrett et al. 2000) are systematically 0.33 mag fainter; such offset becomes stronger towards fainter magnitudes. However, in Fig. 4 we do not find such effect. This can be explained by the fact that Schombert & Smith (2012) covered galaxies in a wider range in

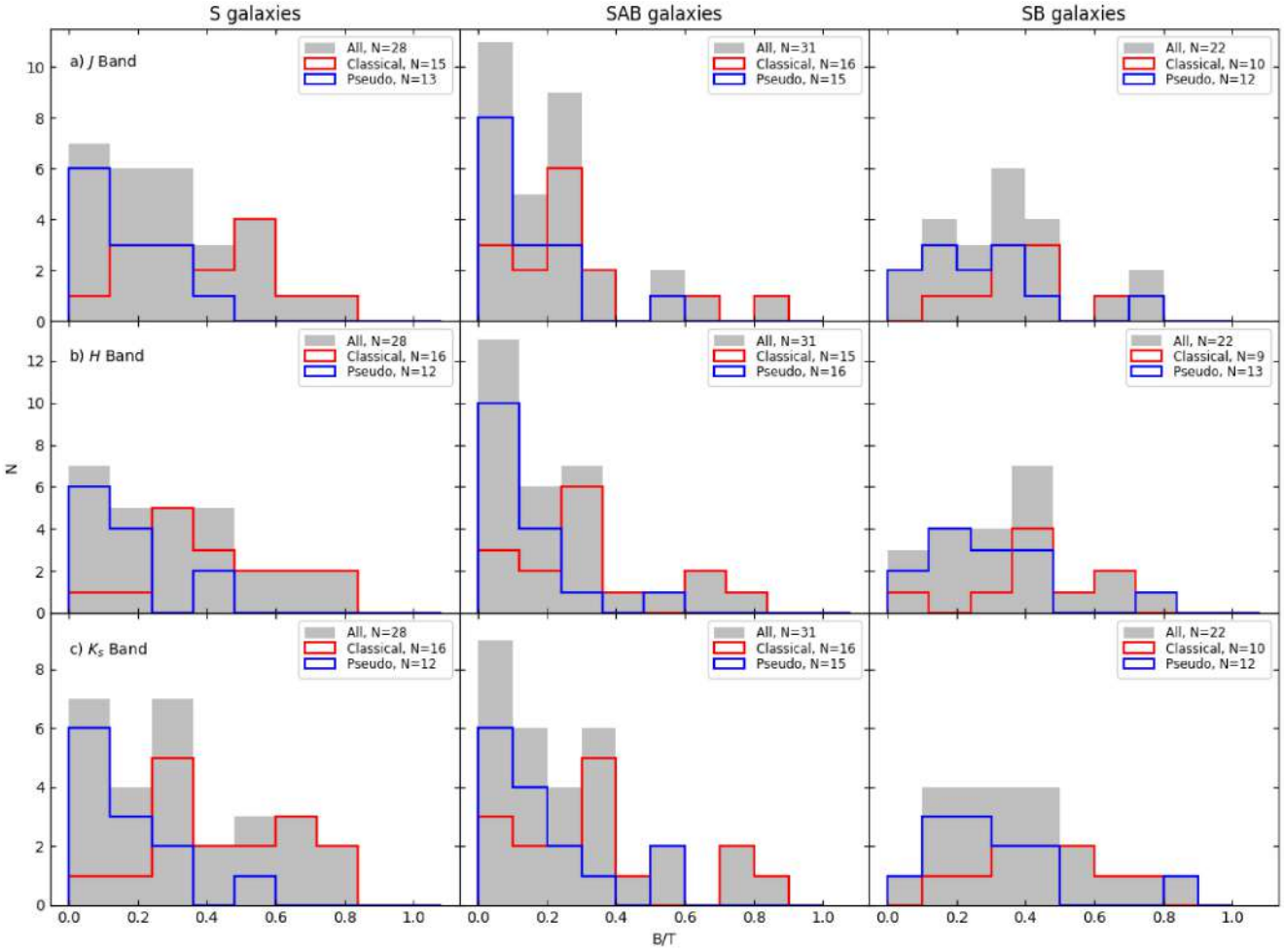

Figure 13. Distribution of the *B*/*T* ratio for spiral galaxies. Panels are from top to bottom: a) *J*, b) *H*, and c) K_s bands, respectively. From left to right: S, SAB, and SB Hubble types, respectively. Colours for histograms are the same as in Fig. 10.

Table 2. Distribution of *n* and *B*/*T*. Columns: (1) Group or subgroup of the sample: *All* stands for the whole sample or subsample, while subscripts *C* and *P* are for classical and pseudo-bulges, respectively. (2)–(4) Mean Sérsic index and (5)–(7) Mean *B*/*T* in 2MASS bands.

Group (1)	$<n>_J$ (2)	$<n>_H$ (3)	$\langle n\rangle_{Ks}$ (4)	$<B/T>_J$ (5)	$<B/T>_H$ (6)	$<B/T>_{Ks}$ (7)
All	2.77 ± 0.15	2.82 ± 0.18	2.98 ± 0.17	0.36 ± 0.03	0.36 ± 0.02	0.38 ± 0.03
All_C	3.49 ± 0.22	3.55 ± 0.22	3.66 ± 0.24	0.46 ± 0.03	0.45 ± 0.03	0.47 ± 0.03
All_P	1.66 ± 0.15	1.72 ± 0.17	1.88 ± 0.25	0.21 ± 0.03	0.22 ± 0.03	0.25 ± 0.04
E+S0	4.70 ± 0.46	4.57 ± 0.50	4.67 ± 0.48	0.64 ± 0.05	0.58 ± 0.06	0.62 ± 0.06
$E+S0_C$	4.82 ± 0.46	4.66 ± 0.51	4.78 ± 0.50	0.64 ± 0.05	0.59 ± 0.07	0.63 ± 0.06
Spirals	2.28 ± 0.14	2.44 ± 0.14	2.55 ± 0.18	0.29 ± 0.02	0.30 ± 0.02	0.33 ± 0.03
$Spirals_C$	2.87 ± 0.19	3.04 ± 0.17	3.17 ± 0.22	0.36 ± 0.03	0.38 ± 0.03	0.40 ± 0.03
$Spirals_P$	1.64 ± 0.15	1.78 ± 0.18	1.86 ± 0.25	0.20 ± 0.03	0.22 ± 0.03	0.24 ± 0.04
S	2.51 ± 0.19	2.68 ± 0.20	2.70 ± 0.22	0.33 ± 0.04	0.34 ± 0.05	0.36 ± 0.05
S_C	3.02 ± 0.18	3.22 ± 0.19	3.24 ± 0.17	0.39 ± 0.06	0.41 ± 0.05	0.41 ± 0.06
S_P	1.92 ± 0.28	1.96 ± 0.29	1.85 ± 0.38	0.24 ± 0.07	0.24 ± 0.07	0.26 ± 0.08
SAB	2.36 ± 0.23	2.47 ± 0.22	2.46 ± 0.24	0.22 ± 0.03	0.23 ± 0.04	0.27 ± 0.04
SAB_C	2.79 ± 0.32	2.92 ± 0.28	2.85 ± 0.28	0.28 ± 0.05	0.33 ± 0.05	0.37 ± 0.06
SAB_P	1.82 ± 0.27	1.93 ± 0.29	2.05 ± 0.38	0.11 ± 0.02	0.12 ± 0.02	0.17 ± 0.04
SB	1.89 ± 0.30	2.07 ± 0.31	2.49 ± 0.50	0.34 ± 0.04	0.35 ± 0.04	0.37 ± 0.04
SB_C	2.79 ± 0.49	2.95 ± 0.46	3.55 ± 0.78	0.42 ± 0.06	0.43 ± 0.06	0.45 ± 0.06
SB_P	1.13 ± 0.13	1.46 ± 0.32	1.62 ± 0.54	0.28 ± 0.05	0.29 ± 0.05	0.31 ± 0.06

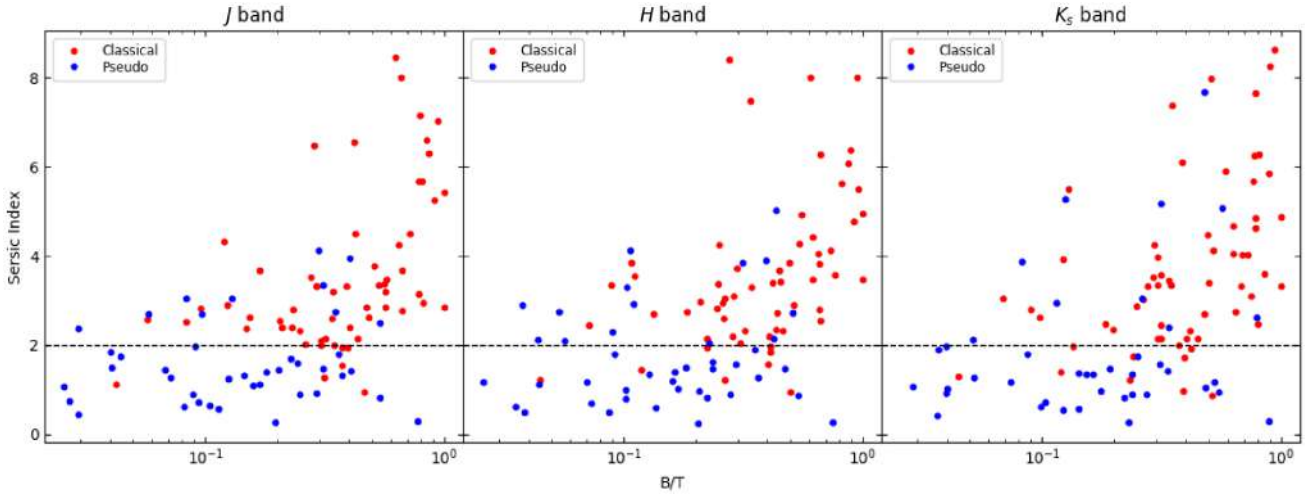

Figure 14. Relation between *B*/*T* and Sérsic index for the galaxies in our sample. According to our classification for bulges, red points represent classical bulges, while the blue ones are pseudo-bulges. Horizontal dashed lines indicate $n = 2$.

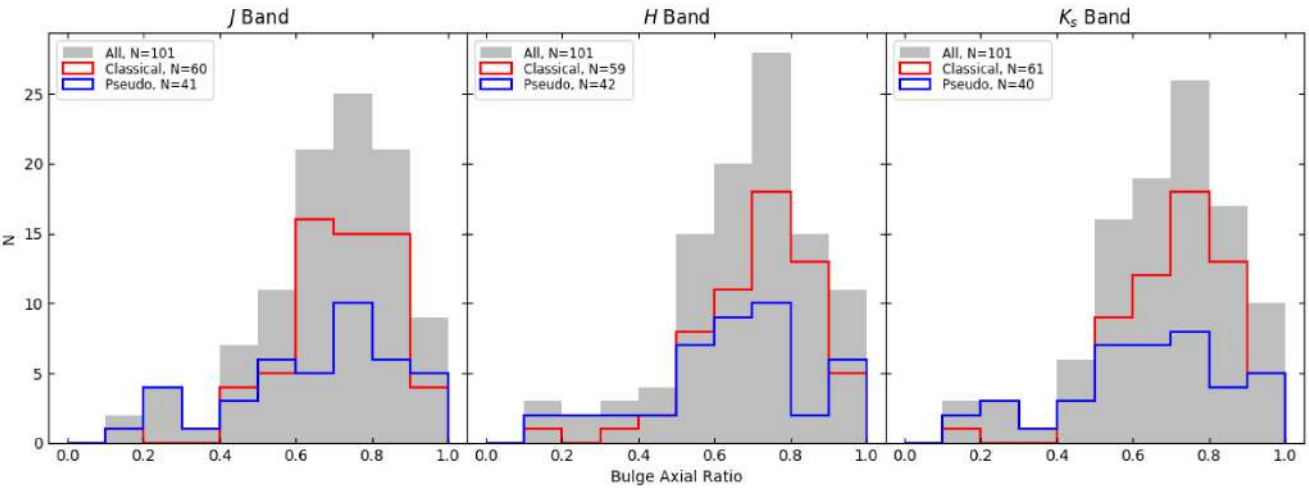

Figure 15. Distribution of the axial ratio q for the galaxies in our sample.

magnitude than us. Mezcua et al. (2018), also using GALFIT to model the surface brightness of galaxies, reported the same discrepancy among their magnitudes with those from 2MASS XSC, which became larger for fainter galaxies. The source of this discrepancy lies on the generation of the LGA mosaics, which affected ETGs strongly. However, we have shown in Fig. 3 that for LTGs, the LGA mosaics can be used safely.

With respect to the comparisons for Sérsic index and effective radius for bulges shown in Figs 7 and 8, these results are consistent. We should point out that Laurikainen et al. (2004a) used a 2D modelling of surface brightness similarly to us. In addition, we are able to recover some well-established correlations that will be presented below.

As mentioned earlier, we have divided bulges into two different groups due to their properties that are related to different formation processes, though indications of different bulge populations were found observationally. Classical bulges have similar properties as elliptical galaxies, while the pseudo-bulges resemble discs; i.e. they have disc-like structure (for reviews, see Kormendy & Kennicutt 2004; Kormendy & Ho 2013). Then, it is expected that pseudo-bulges do not follow the same relations as E galaxies and classical bulges. As we said before, ∼60 per cent of the sample is classified as classical bulges. As the sample analysed in this paper is not complete in magnitude or volume, the distribution of bulges is somewhat biased. Nevertheless, since we have covered a wide galaxy morphology range (from E to SB galaxies), the properties of bulges and pseudo-bulges reported in this paper might be useful to anchor and compare with other galaxies samples at low-z and high-z, in the NIR and other wavelengths. In particular, for large-scale structure and the relation of SMBHs with their host galaxies studies, for which the accurate measurements of structural parameters is highly valuable.

Considering the KR, one of the criteria used to separate bulge types, we found agreement with previous studies (Kormendy 1977; Pahre, Djorgovski & de Carvalho 1995; Añorve 2012; Olguín-Iglesias et al. 2016). Also, Schombert (2013) studied a sample of elliptical galaxies from 2MASS arriving at similar KR parametrization. In addition, in Fig. 9 most of the pseudo-bulges are falling outside of the correlation, which can be attributed to the distinct physical origin of pseudo-bulges that we outlined above. Additionally, we found that a significant amount of $n < 2$ fall as outliers in the KR: for the *J* band,

the 63 per cent pseudo-bulges according to KR have $n < 2$, while for the H and K_s bands, we found the 52 per cent and 68 per cent, respectively; this is in agreement with the results of Gadotti (2009) and Añorve (2012). Our results also show that some pseudo-bulges can be consistent with FP correlations and have larger effective radii and fainter surface brightness at the effective radius (Kormendy & Ho 2013), and some pseudo-bulges are more compact than the classical bulges of the same luminosity (Kormendy & Bender 2012).

Another issue to highlight in our bulges classification is the presence of pseudo-bulges as a function of Hubble type, in the sense that pseudo-bulges are dominant towards LTGs (see Figs 10–13). As we stated above, about 40 per cent of the objects in the entire sample are classified as pseudo-bulges, but when we remove the E+S0 galaxies from the whole sample, about 50 per cent of the spiral (S) galaxies host pseudo-bulges (see panel *c* in Figs 10 and 12). Focusing on each spiral type and depending on the 2MASS band (see Figs 11 and 13), for S galaxies about 44 per cent of bulges are pseudo, while for SAB type about 51 per cent have pseudo-bulges and for barred galaxies the fraction of pseudo-bulges increases up to 56 per cent.

Also, from Figs 10–13 and Table 2, it can be seen that there is a correspondence between the Sérsic index and bulge-to-total (B/T) ratio with Hubble types, since such parameters tend to be higher for ETGs (see panels *b* in Figs 10 and 12). We also confirm the same trend for bulge types; i.e. classical bulges show higher values for n and B/T than pseudo-bulges. Furthermore, in our data it is evident a bimodality in such parameter distributions in the context of bulge types, especially in n, since the overlap is larger in B/T distributions. This bimodality in n, as well as in B/T, has been noticed in previous results (e.g. Allen et al. 2006; Fisher & Drory 2008; Gadotti 2009).

Thus, the average value of Sérsic index when the complete sample (panel *a* in Fig. 10) is considered is about 2.8 (taking into account the three 2MASS bands for which results are very similar to each other). For the other subgroups like E+S0 and spiral galaxies (panels *b* and *c* in Fig. 10, respectively), $<n> \sim 4.6$ and 2.4, respectively. From here, we see that the E+S0 galaxies tend to have higher Sérsic indices than the whole sample and spiral galaxies (these last two groups tend to present similar values between them because most of the objects in our sample are spiral galaxies). These results agree with the expectation that ETGs tend to have high n values (for instance, historically the shapes of the light profiles for E galaxies are well described with the de Vaucouleurs function), while bulges in LTGs usually display low values of Sérsic indices (bearing in mind that disc galaxies can be well modelled with an exponential profile). Besides, if we focus on the peaks of distributions, it can be noticed again that n is higher for E+S0 galaxies, since the peak is ∼4 and higher, while in spiral galaxies and the whole sample the peaks are about 2.5, even though in the K_s band the peaks are at ∼1.5, which is in agreement with previous works where peaks of n distributions range from 1 to 1.3 (e.g. Blanton et al. 2003; Añorve 2012). Thus, we also confirm, as previous studies, the variation of Sérsic index along the Hubble types of galaxies (e.g. Graham 2001; Fisher & Drory 2008). The same behaviour prevails when S galaxies are separated in groups; i.e. early-type systems in spirals, like the bulges of S galaxies, tend to show higher mean values and peaks in their distributions of n than SAB and SB groups (see Fig. 11).

In the context of bulge types, it becomes clear from the plots how these two bulge populations display a division between them. When we consider the entire sample, the average values of $<n> \sim 3.6$ for classical bulges and $<n> \sim 1.8$ for pseudo-bulges. For E+S0 galaxies, we have $<n> \sim 4.8$ for classical bulges (only one E+S0 object was classified as pseudo-bulge; see Section 5.1). For spiral galaxies, we report average values for $<n> \sim 3$ for classical bulges and $<n> \sim 1.7$ for pseudo-bulges. We also found that classical bulges have the following Sérsic index distribution: $<n> \sim 3.2$ for S galaxies, $<n> \sim 2.8$ for SAB galaxies, and $<n> \sim 2.9$ for SB galaxies; however, for pseudo-bulges the values of n are distributed in the following manner: $<n> \sim 1.9$ for S galaxies, $<n> \sim 1.9$ for SAB galaxies, and $<n> \sim 1.4$ for SB galaxies. Our results indicate that in all cases classical bulges have larger n than pseudo-bulges. Also, we observe again a similar trend in the sense that classical bulges in ETGs exhibit higher Sérsic indices than those from LTGs. The same trend prevails for the bulges of S, SAB, and SB groups. For instance, Fisher & Drory (2008) found average $<n> = 3.49$ for classical bulges and $<n> = 1.69$ for pseudo-bulges for a sample of galaxies ranging in Hubble type from S0 to Sc, which also compares in size with ours. Besides, when they add elliptical galaxies to the classical bulges subsample, the value increases to $<n> \sim 3.78$.

Regarding the distributions of B/T, we can see also how it varies as a function of the Hubble type as the case for n, where ETGs tend to have higher values than those in LTGs (see Figs 12 and 13). This drop in B/T values is consistent with previous works (e.g. Graham 2001; Laurikainen, Salo & Buta 2004b; Méndez-Abreu et al. 2017). Analogously to Sérsic index, B/T distribution is bimodal despite the overlap is larger than that in the case of n. The average value of B/T, considering the three bands, is $<B/T> \sim 0.37$ for the complete sample; however, the E+S0 and spiral subgroups show mean values of $<B/T> \sim 0.61$ and 0.30, respectively (see panels *a*, *b*, and *c* in Fig. 12 for each galaxy group). If we see the subsamples of spiral galaxies separately for each 2MASS band (see panels *a*, *b*, and *c* in Fig. 13), then $<B/T> \sim 0.34$ for S galaxies, $<B/T> \sim 0.24$ for SAB galaxies, and $<B/T> \sim 0.34$ for SB galaxies, respectively.

For pseudo-bulges in the whole sample, these tend to have lower values of $<B/T> \sim 0.23$, while classical bulges have $<B/T> \sim 0.46$. The classical bulges of E+S0 galaxies have $<B/T> \sim 0.62$ (again, we recall that there is one object classified as pseudo-bulge in the E+S0 subsample; see Section 5.1). For the group of spirals, the average value of $<B/T> \sim 0.38$ for classical bulges, while for pseudo-bulges it is $<B/T> \sim 0.22$. Again, we see that classical bulges display higher B/T values than pseudo-bulges. The same trend is observed in the bulges of S, SAB, and SB galaxies. Thus, our findings are in good agreement with previous ones reported, such as those values from Fisher & Drory (2008) of $<B/T> = 0.41$ for classical bulges and 0.16 for pseudo-bulges. Besides, similarly to Gadotti (2009), the peak in our distributions for pseudo-bulges is ∼0.10, while for classical bulges it is ∼0.50 (see Fig. 12).

Our results show that most of pseudo-bulges have low values of B/T, while classical bulges cover almost the entire range of B/T distribution. This result is consistent with the one of Fisher, Drory & Fabricius (2009), who reported that pseudo-bulges are more likely to be found in low-B/T galaxies. Our results also show a large overlap in B/T distribution of bulges and pseudo-bulges, confirming that a low B/T value does not secure that a galaxy hosts a pseudo-bulge, and that if a bulge has a $B/T \geq 0.5$, then it can be expected to be classical (e.g. Kormendy & Kennicutt 2004; Kormendy & Ho 2013). Besides, even if some pseudo-bulges can have $B/T > 0.2$ (Fisher & Drory 2008), in our data it is visible how the number of pseudo-bulges decreases towards $B/T \sim 0.5$. A similar behaviour is shown in the distribution of B/T by Peebles (2020), who compiled a sample of mostly disc galaxies from literature (Kormendy et al. 2010; Fisher & Drory 2011). Furthermore, for the galaxies in common with Peebles (2020) we performed a Kolmogorov–Smirnov test and obtained a statistic of 0.35 at the 95 per cent significance level; hence, we retain the null hypothesis and conclude that both B/T data sets are drawn from the same

parent distribution. In fact, from the ∼40 pseudo-bulges in our sample in the three bands of 2MASS, we found that about 12 per cent of them have $B/T \geq 0.5$. Additionally, we find a good agreement with theoretical predictions of semi-analytical models by Izquierdo-Villalba et al. (2019), who show some bulge properties such as B/T for both populations of bulges. The distribution of pseudo-bulges agrees with ours, although they do not fully reproduce the peak towards $B/T \sim 0.1$. None the less, in the case of classical bulges differences arise, since the B/T distribution peaks about 0.1 and abruptly decreases towards values close to 0.5, which, as we said above, is an observed threshold for delimiting bulge types that our results also confirm. Izquierdo-Villalba et al. (2019) argue that this effect is because their model produces classical bulges in galaxies with too-massive stellar discs.

The relation between B/T and Sérsic index in Fig. 14 shows that most of classical bulges tend to locate in the upper region of these plots, presenting larger values for n and B/T. On the other hand, pseudo-bulges tend to present lower values for these parameters. Also, we can see some pseudo-bulges with high values of B/T and $n \geq 2$ and, conversely, some classical bulges with low values of B/T and $n < 2$. This result confirms what we have said before about the distribution for these parameters and is in agreement with previous works (e.g. Laurikainen et al. 2004b; Fisher & Drory 2008; Gadotti 2009; Weinzirl et al. 2009). Nevertheless, a correlation between Sérsic index and B/T is weak at the most, especially for pseudo-bulges. We further discuss the properties and tendencies displayed by pseudo-bulges, classical bulges, and elliptical galaxies in the companion paper.

Therefore, we can conclude that our results also show a bimodality present in the distributions for n and, to a lesser extent, for B/T. Fig. 14 shows that classical bulges and pseudo-bulges cannot be distinguished using B/T alone, and that the $n \geq 2$ threshold provides a better separation. Thus, contrary to Kormendy & Ho (2013), we state that B/T cannot be used as a single bulge classifier in the NIR.

Similarly, the distribution of the axial ratio q for bulges does not display a clear separation between pseudo-bulges and classical bulges; in fact, both distributions look practically indistinguishable, showing a very extended overlap in almost all the dynamic range (see Fig. 15). The peaks of distributions are located at $q \sim 0.8$ in the three bands. This result is qualitatively in agreement with previous works (e.g. Padilla & Strauss 2008; Bruce et al. 2012).

According to Kormendy & Kennicutt (2004), the morphology of bulges can be used as a criterion to distinguish between bulges, since pseudo-bulges tend to have a disc-like morphology; i.e. they show an apparent flattening similar to that of the outer disc. Thus, we would expect to see more pseudo-bulges with lower q than classical bulges. However, this tendency is barely seen in Fig. 15 in the low-amplitude tails when q tends to zero.

5.1 Notes on individual galaxies

We will discuss below some cases related to their bulge classifications. First, we consider the galaxy M110 that has been classified as a pseudo-bulge following the criteria of KR and low velocity dispersion; in fact, it is an extreme outlier of the KR and the only ETG classified as a pseudo-bulge (see Fig. 9). This object is a dwarf elliptical galaxy classified also as peculiar (E5,pec; de Vaucouleurs et al. 1991). M110 and M32 are satellites of M31. Evidence suggests that substantial stellar material (found in the halo of M31) has been stripped from these satellite galaxies after tidal interactions with M31 (Ibata et al. 2001). As a matter of fact, Jarrett et al. (2003) also pointed out the particular case of M110, arguing that its radial surface brightness is dominated by an exponential disc, which reinforces the issue that M110 was fitted with two components (see Section 4.1.1). Regarding the compact elliptical galaxy M32 (cE2), it is classified as classical bulge because of the KR and n criteria, and, similarly to M110, it was modelled with two components [an exponential disc as an additional component; actually, Graham (2002) reported that its surface brightness distribution is well described by a bulge plus an exponential disc profile]. Besides, it has been proposed that it was a disc galaxy with initial luminosity close to that of our Galaxy, which was disrupted due to an encounter with the Andromeda galaxy (D'Souza & Bell 2018). So, this may be the reason why M32 is falling almost in the 3σ boundary of the KR (see Fig. 9). Hence, the low values in surface brightness, Sérsic index, and velocity dispersion of M110, as well as the case of M32, can be a consequence of tidal interactions with M31.

We have a few cases (only 4 per cent of the sample) where the bulge classification does not arrive at the same bulge type in the three NIR bands. The galaxies with discrepant classification are the following: NGC 4710, NGC 3344, M51b, and NGC 7582. We decided to assign as the final classification the one that was common in the two other bands. Thus, the bulge of NGC 4710 is classified as classical in the H and K_s bands, while the one of NGC 3344 is classified as a pseudo-bulge only in the H band. On the other hand, the bulge of M51b is a pseudo-bulge in bands J and H, while the bulge of NGC 7582 is classified as a pseudo-bulge in the H and K_s bands.

In addition, the galaxies M83 and NGC 5792, lacking reported velocity dispersion data, do not fit into either of the two bulge categories. These galaxies have $n < 2$ and do follow the KR, but to assign a classification, we considered less established properties of pseudo-bulges, such as B/T ratio and the presence of bars within the bulge region (Fisher & Drory 2008), since M83 (SAB) and NGC 5792 (SB) are barred galaxies and have $B/T \lesssim 0.20$. Hence, our final classification is that the bulges in M83 and NGC 5792 are pseudo-bulges.

We have also compared our bulge classifications with some previous works. For instance, we have 10 disc galaxies in common with Kormendy & Ho (2013); 6 of them are classical bulges and the other 4 are pseudo-bulges. We agree on the classical bulges; however, we disagree on the classification of NGC 4826 and NGC 4945 as pseudo-bulges. Kormendy & Ho (2013) used more classification criteria than us (the list was introduced by Kormendy & Kennicutt 2004, and an object must hold at least two of them). After inspecting such list given also by Kormendy et al. (2011), we noticed that the bulge of NGC 4826 was classified as a pseudo-bulge because the centre of the galaxy is dominated by Population I material and there is no sign of a merger in progress; besides, NGC 4826 is rotation dominated and is a low-σ outlier in the Faber–Jackson relation (FJR) according to Kormendy et al. (2011). However, for us NGC 4826 follows the KR; it has $n > 2$ and $\sigma = 96\ \mathrm{km\,s^{-1}}$ (in fact, they also report such σ value). Nevertheless, in a plot of the FJR (Paper II), it can be seen that it is not a low-σ outlier. As we see, velocity dispersion information is the only point in common we do agree with, so a possible explanation for this discrepancy may be related to the difference in the surface brightness modelling, since 1D decomposition was used by Kormendy & Ho (2013), unlike the 2D approach presented in this paper.

Regarding NGC 4945, a barred galaxy viewed edge-on with a dusty bulge, we failed to find the criteria by which it was classified as a pseudo-bulge. However, it is also considered as a pure-disc galaxy viewed edge-on that contains neither a classical nor a pseudo-bulge (Kormendy et al. 2011). Nevertheless, we found that the bulge of NGC 4945 is more prominent in the K_s band. Then, we have classified NGC 4945 as a classical bulge due to its $n > 2$ and $\sigma > 130\ \mathrm{km\,s^{-1}}$, in spite of being an outlier in the KR.

Also, when comparing with the identification of bulge types performed by Fisher & Drory (2008), we found that from the 16 galaxies in common, only 3 bulges are classical and the rest are labelled as pseudo-bulges. We agreed on the three classical bulge classifications, but disagree on seven of the pseudo-bulges. We disagree on the pseudo-bulge type assigned to the bulges of the galaxies NGC 4826, NGC 3166, NGC 4569, NGC 4579, M63, M88, and M106 (the latter one is classified as a classical bulge by us, in agreement with Kormendy & Ho 2013). Fisher & Drory (2008) classifications are based on the morphology of the galaxy in the bulge region, which is the only classification criterion used. If the bulge contains a nuclear bar, a nuclear spiral, and/or a nuclear ring, it is classified as a pseudo-bulge by Fisher & Drory (2008). None the less, as has been shown in previous studies (e.g. Graham 2008; Kormendy & Ho 2013) and in this paper, barred galaxies can host classical bulges. This supports the view that using a single criterion as suggested by Fisher & Drory (2008) may not be sufficient to classify bulges in barred galaxies (e.g. Erwin et al. 2021).

The disagreements discussed here suggest that a more detailed inspection for these galaxies may be required, since they may contain peculiar bulges, which in turn indicates that our classification scheme may be incomplete. Thus, we should mention that in this paper we are currently unable to classify bulges that may be composite systems, with both pseudo-bulge and classical bulge features, that may co-exist in the bulges of some galaxies (Kormendy & Kennicutt 2004; Kormendy & Ho 2013); for example, the bulge of NGC 4826 was classified as a mixed bulge by Kormendy et al. (2010). Complementary dynamical studies could be useful to explain the nature of composite pseudo-classical bulges [e.g. Erwin et al. (2021) presented a very complete analysis combining photometry with IFU stellar kinematics]. Such studies may help us to establish more robust criteria for recognizing between different types of bulges.

6 SUMMARY AND CONCLUSIONS

In this work, we studied a sample of bright and nearby galaxies by modelling their surface brightness through a 2D photometric decomposition in order to obtain information about their structural parameters. This sample of galaxies spans from early- to late-type morphologies. We remind the reader that measured parameters from our 2D photometric decomposition carried out with GALFIT are presented in tables available only in digital format. We have compared our results obtained with previous works using a 1D technique and we found consistency in them. Besides, we have looked into the issue related to the 2MASS galaxy photometry. Also, from a joint analysis between structural parameters, scaling relations, and kinematic measurements (the latter information taken from the literature), we classified bulges in galaxies into classical bulges and pseudo-bulges. We summarize our main conclusions as follows:

(i) We performed a 2D surface brightness modelling for the galaxies in our sample using GALFIT. The sample comprises 101 bright and nearby galaxies observed by the 2MASS survey in the NIR bands. From this analysis, we obtained information for the structural parameters of galaxies, such as concentration indices, effective radii, magnitudes, and axial ratios, among others.

(ii) The 2D photometric decomposition carried out in this work has been more detailed than other works, in the sense that many of them at most include a bulge + disc decomposition, while our models generated with GALFIT go further by considering a bar and an additional component in some cases. Similarly, many of the elliptical galaxies in our sample are described by models involving a Sérsic component plus an additional component. We show that in the NIR the inner component suggested by Huang et al. (2013a) is absent. This might be related to the difference in stellar populations that are sampled in optical, which differ in the NIR.

(iii) We have addressed the sky oversubtraction issue related to the 2MASS data for the LGA mosaics, where the outer region of large ETGs was removed by using an aperture that was too close to the galaxy during the mosaic construction. Alternatively, we used the IRSA tile service to generate images to perform comparisons between both data sets, i.e. LGA mosaics and image tiles. In Section 3.6, we demonstrated that the oversubtraction problem present in the LGA mosaics affected ETGs strongly, while LTGs were unaffected. The total magnitudes measured on LGA mosaics presented a mean offset of 0.32, 0.34, and 0.34 mag for J, H, and K_s, respectively. Therefore, we propose to use image tiles generated through IRSA server for a more accurate appraisal of the surface brightness photometry for ETGs, instead of using LGA mosaics.

(iv) We have compared our results with published 1D photometric analyses, finding close agreement. Nevertheless, our 2D approach considers more degrees of freedom, allowing us to disentangle the contributions of different galaxy components, such as bulge, disc, and bar, in a more reliable fashion. This also allows us to recover some well-established correlations between structural parameters of galaxies.

(v) As it has been suggested in many studies (e.g. Kormendy & Ho 2013; Fisher & Drory 2016), the use of only one criterion alone to identify bulge varieties does not provide a robust classification. Therefore, we use the following criteria: the KR, Sérsic index, and velocity dispersion. We consider as pseudo-bulges those points falling as outliers in KR. Also, a low Sérsic index, $n < 2$, could be an indicator of pseudo-bulge; otherwise, if $n \geq 2$, it is considered as a classical bulge. Regarding the velocity dispersion, if a bulge has a velocity dispersion < 130 km s^{-1}, it is likely to be a pseudo-bulge, while above this threshold it would be regarded as a classical bulge. Hence, if one object holds at least two of these conditions, it is classified as classical bulge or pseudo-bulge. Thus, we obtained that ∼40 per cent of the sample is classified as pseudo-bulges in the three bands of 2MASS.

(vi) Our results confirm the previous distributions for some properties of classical bulges and pseudo-bulges, such as Sérsic index, B/T ratio, and q ratio (e.g. Fisher & Drory 2008; Kormendy & Ho 2013). The bimodality is more evident for n, while for B/T ratio the overlap between classical and pseudo-bulges is large. For this reason, we did not use the B/T ratio as an auxiliary criterion for bulge classification. Our results indicate that classical bulges and ETGs tend to have higher values of n and B/T than pseudo-bulges and LTGs. Similarly, in the axial ratio distribution is evident even a more extended overlap between bulge types in almost all the dynamic range; only towards low values of q ratio, we can marginally see a trend in which the presence of pseudo-bulges increases. We found that, to a greater extent, pseudo-bulges tend to be found in LTGs, since the fraction of pseudo-bulges increases from S to SB galaxies.

(vii) We also made a direct comparison of our bulge classification for objects in common with previous studies (Fisher & Drory 2008; Kormendy & Ho 2013). In general, we agreed on the classifications of classical bulges, but disagreed in some cases that were classified as pseudo-bulges. The classification scheme advanced in this paper does not include composite systems, i.e. those bulges sharing classical bulge/pseudo-bulge features. Thus, a more refined classification might need to include IFU complementary kinematic information.
In a companion paper, we explore some of the most common galaxy scaling relations for the sample presented in this paper, as well as

correlations between the mass of SMBH and global properties of the galaxies.

ACKNOWLEDGEMENTS

We are very grateful to the anonymous referee for very constructive comments and for pointing out the background oversubtraction problem on 2MASS LGA mosaics. ER-L is grateful to Mexico's National Council of Science and Technology (CONACYT) for supporting this research under PhD studentship grant and to Elena Terlevich for the SNI–CONACYT graduate assistantship. JA-E, MV, and GI are grateful to *Verano de la Investigación Científica en el INAOE (VICI)*, an INAOE's Summer Research Programme sponsored by the Mexican Academy of Sciences (AMC), Programa DELFIN, CONACYT, and INAOE. We wholeheartedly thank Prof. Tom Jarrett for sharing 2MASS reduced, star-removed, data cubes and for all the useful discussions that helped us to improve this paper. We thank Prof. James Schombert for sharing data and for the useful exchange of ideas. We also thank ELT Ramondavid Ríos Lopez for proofreading the article. Last but not least, we want to express our most gratitude to Chien Peng for his constant, helpful, and friendly advice on the use of GALFIT, all along the different stages of our project.

This publication makes use of data products from the 2MASS, which is a joint project of the University of Massachusetts and the Infrared Processing and Analysis Center/California Institute of Technology, funded by the National Aeronautics and Space Administration and the National Science Foundation. This research has made use of the NASA/IPAC Extragalactic Database, which is funded by the National Aeronautics and Space Administration and operated by the California Institute of Technology. We acknowledge the usage of the HyperLeda database (http://leda.univ-lyon1.fr).

DATA AVAILABILITY

The data underlying this paper are available in tables and online supplementary material. Other data sets were derived from sources in the public domain: 2MASS LGA at https://irsa.ipac.caltech.edu/applications/2MASS/LGA/, 2MASS image tiles at https://irsa.ipac.caltech.edu/applications/2MASS/IM/interactive.html#pos, NASA Extragalactic Database at http://ned.ipac.caltech.edu/, and Hyperleda data base at http://leda.univ-lyon1.fr/leda/param/vdis.html.

REFERENCES

Akaike H., 1974, IEEE Trans. Autom. Control, 19, 716
Allen P. D., Driver S. P., Graham A. W., Cameron E., Liske J., de Propris R., 2006, MNRAS, 371, 2
Añorve C., 2012, PhD thesis, INAOE
Añorve C., 2020, Canorve/EllipSect: Release of EllipSect, available at https://zenodo.org/record/4050352
Athanassoula E., 2005, MNRAS, 358, 1477
Athanassoula E., Morin S., Wozniak H., Puy D., Pierce M. J., Lombard J., Bosma A., 1990, MNRAS, 245, 130
Barden M., Häußler B., Peng C. Y., McIntosh D. H., Guo Y., 2012, MNRAS, 422, 449
Bertin E., Arnouts S., 1996, A&AS, 117, 393
Binney J. J., Davies R. L., Illingworth G. D., 1990, ApJ, 361, 78
Blanton M. R. et al., 2003, ApJ, 594, 186
Blanton M. R., Kazin E., Muna D., Weaver B. A., Price-Whelan A., 2011, AJ, 142, 31
Bonfini P., 2014, Publ. Astron. Soc. Pac., 126, 935
Bruce V. A. et al., 2012, MNRAS, 427, 1666
Caon N., Capaccioli M., D'Onofrio M., 1993, MNRAS, 265, 1013
Capaccioli M., 1989, in Corwin H. G. J., Bottinelli L., eds, World of Galaxies (Le Monde des Galaxies). Springer-Verlag, New York, NY, p. 208
Cappellari M. et al., 2011, MNRAS, 413, 813
Cappellari M. et al., 2013, MNRAS, 432, 1709
Chilingarian I. V., Melchior A.-L., Zolotukhin I. Y., 2010, MNRAS, 405, 1409
D'Souza R., Bell E. F., 2018, Nat. Astron., 2, 737
de Jong R. S., 1996a, A&AS, 118, 557
de Jong R. S., 1996b, A&A, 313, 377
de Jong R. S., van der Kruit P. C., 1994, A&AS, 106, 451
de Vaucouleurs G., 1948, Ann. Astrophys., 11, 247
de Vaucouleurs G., de Vaucouleurs A., Corwin Herold G. J., Buta R. J., Paturel G., Fouque P., 1991, Third Reference Catalogue of Bright Galaxies. Springer, New York, NY
Djorgovski S., Davis M., 1987, ApJ, 313, 59
Dullo B. T., Graham A. W., 2013, ApJ, 768, 36
Erwin P. et al., 2021, MNRAS, 502, 2446
Eskridge P. B. et al., 2002, ApJS, 143, 73
Faber S. M., Jackson R. E., 1976, ApJ, 204, 668
Fisher D. B., Drory N., 2008, AJ, 136, 773
Fisher D. B., Drory N., 2011, ApJ, 733, L47
Fisher D. B., Drory N., 2016, in Laurikainen E., Peletier R., Gadotti D., eds, Astrophysics and Space Science Library, Vol. 418, Galactic Bulges. Springer Int. Publ., Switzerland, p. 41
Fisher D. B., Drory N., Fabricius M. H., 2009, ApJ, 697, 630
Freeman K. C., 1970, ApJ, 160, 811
Frogel J. A., Quillen A. C., Pogge R. W., 1996, in Block D. L., Greenberg J. M., eds, Astrophysics and Space Science Library, Vol. 209, New Extragalactic Perspectives in the New South Africa. Kluwer Acad. Publishers, Dordrecht, p. 65
Gadotti D. A., 2008, MNRAS, 384, 420
Gadotti D. A., 2009, MNRAS, 393, 1531
Gao H., Ho L. C., 2017, ApJ, 845, 114
Gao H., Ho L. C., Barth A. J., Li Z.-Y., 2019, ApJS, 244, 34
Graham A. W., 2001, AJ, 121, 820
Graham A. W., 2002, ApJ, 568, L13
Graham A. W., 2008, ApJ, 680, 143
Graham A. W., 2013, in Oswalt T. D., Keel W. C., eds, Planets, Stars and Stellar Systems, Vol. 6. Springer, Dordrecht, p. 91
Greene J. E., Ho L. C., Barth A. J., 2008, ApJ, 688, 159
Häussler B. et al., 2007, ApJS, 172, 615
Ho L. C., Greene J. E., Filippenko A. V., Sargent W. L. W., 2009, ApJS, 183, 1
Huang S., Ho L. C., Peng C. Y., Li Z.-Y., Barth A. J., 2013a, ApJ, 766, 47
Huang S., Ho L. C., Peng C. Y., Li Z.-Y., Barth A. J., 2013b, ApJ, 768, L28
Ibata R., Irwin M., Lewis G., Ferguson A. M. N., Tanvir N., 2001, Nature, 412, 49
Izquierdo-Villalba D., Bonoli S., Spinoso D., Rosas-Guevara Y., Henriques B. M. B., Hernández-Monteagudo C., 2019, MNRAS, 488, 609
Jarrett T., 2004, Publ. Astron. Soc. Aust., 21, 396
Jarrett T. H., Chester T., Cutri R., Schneider S., Skrutskie M., Huchra J. P., 2000, AJ, 119, 2498
Jarrett T. H., Chester T., Cutri R., Schneider S. E., Huchra J. P., 2003, AJ, 125, 525
Jedrzejewski R. I., 1987, MNRAS, 226, 747
Kormendy J., 1977, ApJ, 218, 333
Kormendy J., Bender R., 2012, ApJS, 198, 2
Kormendy J., Ho L. C., 2013, ARA&A, 51, 511
Kormendy J., Kennicutt R. C. J., 2004, ARA&A, 42, 603
Kormendy J., Drory N., Bender R., Cornell M. E., 2010, ApJ, 723, 54
Kormendy J., Bender R., Cornell M. E., 2011, Nature, 469, 374
Lacerna I., Ibarra-Medel H., Avila-Reese V., Hernández-Toledo H. M., Vázquez-Mata J. A., Sánchez S. F., 2020, A&A, 644, A117
Läsker R., Ferrarese L., van de Ven G., 2014, ApJ, 780, 69
Lauer T. R. et al., 2007, ApJ, 662, 808
Laurikainen E., Salo H., Buta R., Vasylyev S., 2004a, MNRAS, 355, 1251
Laurikainen E., Salo H., Buta R., 2004b, ApJ, 607, 103

Ma C.-P., Greene J. E., McConnell N., Janish R., Blakeslee J. P., Thomas J., Murphy J. D., 2014, ApJ, 795, 158
Mannucci F., Basile F., Poggianti B. M., Cimatti A., Daddi E., Pozzetti L., Vanzi L., 2001, MNRAS, 326, 745
Méndez-Abreu J. et al., 2017, A&A, 598, A32
Mezcua M., Hlavacek-Larrondo J., Lucey J. R., Hogan M. T., Edge A. C., McNamara B. R., 2018, MNRAS, 474, 1342
Olguín-Iglesias A. et al., 2016, MNRAS, 460, 3202
Padilla N. D., Strauss M. A., 2008, MNRAS, 388, 1321
Pahre M. A., Djorgovski S. G., de Carvalho R. R., 1995, ApJ, 453, L17
Paturel G., Petit C., Prugniel P., Theureau G., Rousseau J., Brouty M., Dubois P., Cambrésy L., 2003, A&A, 412, 45
Peebles P. J. E., 2020, MNRAS, 498, 4386
Peng C. Y., Ho L. C., Impey C. D., Rix H.-W., 2002, AJ, 124, 266
Peng C. Y., Ho L. C., Impey C. D., Rix H.-W., 2010, AJ, 139, 2097
Ravindranath S., Ho L. C., Peng C. Y., Filippenko A. V., Sargent W. L. W., 2001, AJ, 122, 653
Rix H.-W., Rieke M. J., 1993, ApJ, 418, 123
Schlegel D. J., Finkbeiner D. P., Davis M., 1998, ApJ, 500, 525
Schombert J., 2011, preprint (arXiv:1107.1728)
Schombert J. M., 2013, Publ. Astron. Soc. Aust., 30, e034
Schombert J., Smith A. K., 2012, Publ. Astron. Soc. Aust., 29, 174
Schwarz G., 1978, Ann. Stat., 6, 461
Sérsic J. L., 1963, Bol. Asociacion Argentina Astron. La Plata Argentina, 6, 41
Sérsic J. L., 1968, Atlas de Galaxias Australes. Observatorio Astronomico, Cordoba
Silk J., Di Cintio A., Dvorkin I., 2015, Nuovo Cimento Riv. Ser., 37, 621
Simard L., Mendel J. T., Patton D. R., Ellison S. L., McConnachie A. W., 2011, ApJS, 196, 11
Skrutskie M. F. et al., 1997, in Garzon F., Epchtein N., Omont A., Burton B., Persi P., eds, Astrophysics and Space Science Library, Vol. 210, The Impact of Large Scale Near-IR Sky Surveys. Kluwer Acad. Publ. Co., Dordrecht, p. 25
Skrutskie M. F. et al., 2006, AJ, 131, 1163
Spergel D. N. et al., 2007, ApJS, 170, 377
Springel V. et al., 2005, Nature, 435, 629
Tarsitano F. et al., 2018, MNRAS, 481, 2018
Tully R. B., Fisher J. R., 1977, A&A, 54, 661
Tully R. B., Verheijen M. A. W., Pierce M. J., Huang J.-S., Wainscoat R. J., 1996, AJ, 112, 2471
van der Marel R. P., 1991, MNRAS, 253, 710
Weinzirl T., Jogee S., Khochfar S., Burkert A., Kormendy J., 2009, ApJ, 696, 411
White S. D. M., Rees M. J., 1978, MNRAS, 183, 341

SUPPORTING INFORMATION

Supplementary data are available at *MNRAS* online.

Table 3: Photometry
Table 4: Structural Parameters in J band
Table 5: Structural Parameters in H band
Table 6: Structural Parameters in K_s band

Please note: Oxford University Press is not responsible for the content or functionality of any supporting materials supplied by the authors. Any queries (other than missing material) should be directed to the corresponding author for the article.

APPENDIX A: ESTIMATION OF UNCERTAINTIES FOR GALFIT PARAMETERS

Previous works have shown that GALFIT underestimates errors (e.g. Häussler et al. 2007; Tarsitano et al. 2018). Here, we treat this problem through the model fitting of artificial galaxies. In other words, we have created galaxy images that resemble the 2MASS galaxy images in our sample and then we used GALFIT to fit those galaxies to estimate the parameter errors.

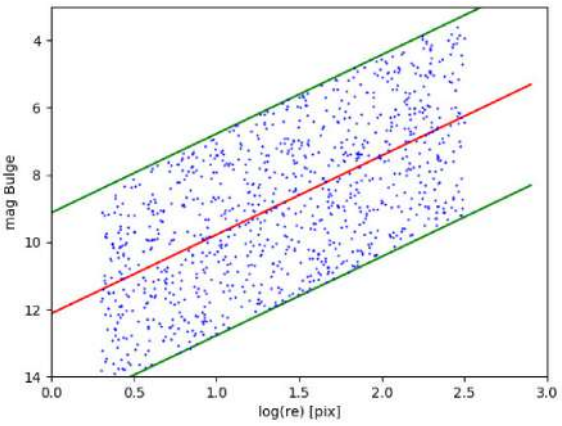

Figure A1. Magnitude–effective radius relation for 1000 simulated galaxies. The *Y*-axis represents apparent magnitude and the *X*-axis represents effective radius in pixels. Blue points represent artificial bulges. Red solid line is the liner fit to the relation taken from our data in the *J* band. Green solid lines represent the limits for the parameters of our artificial galaxies.

An important step to build mock galaxies is to model errors as accurately as possible and identify model parameters that may contribute significantly to errors. Among those main components, we have atmosphere blurring, Poisson error, sky error, and object contamination by nearby objects, such as other galaxies or stars.

As it can be seen in the images, 2MASS galaxies for our sample are brighter than any other object within the same image. This means that objects such as stars (or other galaxies) make little contribution to the errors. This implies that we can construct reliable isolated artificial galaxies since the main galaxy is practically unaffected by other objects of the image. In addition, as it was explained earlier, we use SExtractor to make masks for undesired objects in the image.

Another minor error source to surface brightness modelling is atmosphere blurring. In our 2MASS sample, galaxies are larger than the average PSF (e.g. ∼3.2 arcsec for the *J* band), which implies that the surface brightness model is almost unaffected by PSF's convolution. We have tested this by removing the PSF models during the fits and, as a result, the differences between the model with and without PSFs are minimum (∼0.01 difference in Sérsic index and other cases nearly ∼1). However, as we stated above, we remind the reader that the models generated with GALFIT for the galaxies in our sample are convolved with the PSF image.

We also take into account the error contribution by the sky background, since it may slightly influence the model parameters despite we use observations in NIR bands. In particular, bands *H* and K_s reach values of 1 in σ dispersion (see Table A3). This becomes the main source of errors for our fittings. Below, we explain how we construct and fit artificial galaxies.

A1 Generation of artificial galaxies

We have made isolated galaxies on images of size 500 × 500 pixels for each band of the 2MASS data. This is the smallest size for our 2MASS's images. We have created 1000 galaxy images for each band *J*, *H*, and K_s (i.e. 3000 in total). To construct galaxies, we have modelled them from surface brightness models. As in the fitting procedure for our 2MASS data, Sérsic profile is used for single-

Table A1. Range of parameters used for artificial galaxies (Sérsic component).

Parameter	Min	Max
Flux(mag)	1.8	11.6
Effective radius ($\log r_e$)	0.3	2.5
Sérsic index (n)	0.5	7.0
Axial ratio (q)	0.4	1.0
Position Angle (θ)	− 90.0	90.0

Table A2. Range of parameters used for artificial galaxies (bulge+disc components).

Bulge			Disc		
Parameter	Min	Max	Parameter	Min	Max
mag	3.3	14.1	mag	0.6	12.7
$\log r_e$	0.3	2.5	$\log r_s$	1.0	3.0
n	0.5	7.0	–	–	–
q	0.4	1.0	q	0.1	1.0
θ	− 90.0	90.0	θ	− 90.0	90.0

Table A3. Sky mean values for the sky background and PSF's FWHM.

	Sky		PSF
Band	μ	σ	<FWHM>
J	0.007	0.60	3.20
H	0.002	1.00	3.10
K_s	0.008	1.02	3.14

component galaxies, while Sérsic and exponential models are used for bulge and disc, respectively.

We have obtained the model parameters from the magnitude–effective radius relation result of the simulation process in a similar way as Häussler et al. (2007). For instance, for one galaxy we have selected a random $\log(r_e)$ (in pixels) and computed the magnitude at the effective radius according to the magnitude–effective radius relation that we have obtained from our sample. In Fig. A1 is shown an example of the bulge distribution obtained from our data in the J band.

Tables A1 and A2 summarize the range of parameters used for both Sérsic and bulge+disc artificial galaxies, respectively. Unlike Häussler et al. (2007), we treat the Sérsic index n and sky background as free parameters.

Once we obtained the catalogue file, we proceeded to construct galaxies using GALFIT. The reliability of GALFIT for constructing Sérsic models has been tested before (Häussler et al. 2007). Also, here we focus on testing how the sky noise affects our fits.

We have made a file with the initial parameters for every galaxy in the catalogue. Then, we proceeded to run GALFIT on every file to obtain a galaxy image. This image does not contain any source of noise.

To insert the sky noise, we first estimate the mean and standard deviation in separated regions of the sky (near to the corners; see Table A3) of every 2MASS image. We have selected squares with sizes of 200 x 200 pixels in empty regions.

Using the means of the PSF's FWHM per each band listed in Table A3, Gaussian models were used to replicate the PSF used for convolving with the galaxy model. Then, Poisson noise was also added. As a final step, we have added a template with sky background to this last image.

Table A4. Results from simulations for galaxies with a single Sérsic component.

	Δmag		Δr_e		Δn	
Band	Mean	σ	Mean	σ	Mean	σ
J	− 0.002	0.008	0.037	0.272	− 0.002	0.007
H	0.006	0.008	0.211	0.348	0.002	0.010
K_s	− 0.005	0.068	− 0.210	0.475	− 0.001	0.018

Table A5. Results from simulations for galaxies with bulge and disc components.

	Bulge						Disc			
	Δmag		Δr_e		Δn		Δmag		Δr_s	
Band	Mean	σ	Mean	σ	Mean	σ	Mean	σ	Mean	σ
J	0.040	0.071	− 0.023	0.659	− 0.017	0.076	0.006	0.060	− 0.145	0.612
H	0.030	0.056	0.061	0.556	− 0.005	0.049	0.018	0.075	0.062	0.618
K_s	0.010	0.019	0.605	0.757	− 0.007	0.063	0.020	0.059	− 0.082	0.538

Following, we proceeded to fit the galaxies using GALFIT. We used a small script to automate this process. This script runs SExtractor on each image and adapts its output catalogue to create GALFIT initial parameter files. From the 1000 galaxies in each band, GALFIT was able to fit above 90 per cent of the galaxies in each band for every case of single, bulge, and disc components.

For the case of single Sérsic galaxies, we used two components to fit: a Sérsic model and sky model. On the other hand, for bulge+disc galaxies we used three components: Sérsic, Exponential disc, and sky model.

Sky component was regarded as a free parameter during the fit (as we did with fittings on 2MASS images). Once we have the object file, the script creates a list file that contains the file path of the initial parameter files to run with GALFIT. Finally, we run this list file along with GALFIT.

When GALFIT has finished, we compare the fitted model galaxies with their true model values to estimate the parameter errors. The results are shown in the next section.

A2 Resulting uncertainties

Here, we show the results of the fitting of the simulated galaxies created as it was explained earlier. In Tables A4 and A5 are summarized the results for galaxies with a single Sérsic and bulge+disc components, respectively. The columns show the deviations from the simulated value and scatter for the most important fitting parameters as magnitude, r_e (in pixels), and n. The mean and σ values given are computed after applying a 3σ clipping to those simulated galaxies that were successfully fitted by GALFIT. Hence, the number of galaxies was >80 per cent of the 1000 simulated galaxies in most of the parameters computed. In fact, it can be seen how sky errors (see Table A3) are related to uncertainties reported in Table A4, in the sense that sky dispersion in the K_s band tends to be higher and as a result, the uncertainties for parameters such as magnitude, r_e, and n are also higher.

As it can be noticed in Fig. A2, when we computed the differences between the simulated and the fitted galaxies for these three parameters, there are no significant deviations from the expected values, where a really good parameter recovery can be seen. This agreement is due to the high S/N in the observed galaxies, which is secured by the high flux of the galaxies in our sample ($K_s < 10$; see Fig. 1), the high resolution achieved on each galaxy due to their large size, which makes the effects of seeing almost negligible, and the relative low

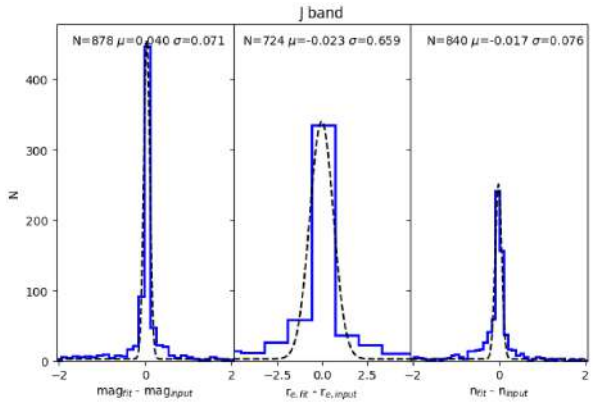

Figure A2. Histograms showing the deviations for the fitting parameters analysed in the simulations, Δmag, Δr_e, and Δn, generated from data in the *J* band for bulges.

deviations in the background that is indicated by the tight parameter recovery. This, however, is not seen in other works when fainter galaxies are considered (e.g. Häussler et al. 2007; Añorve 2012). Hence, final error bars used in the analysis of this work are obtained by adding in quadrature the uncertainties reported in this appendix (Tables A4 and A5) with the ones from GALFIT models reported in Tables 3–6.

This paper has been typeset from a TEX/LATEX file prepared by the author.